Weak imposition of boundary conditions for the boundary element method in the time domain

A. Aimi[1,+], G. Di Credico[1,2,+,*], H. Gimperlein[2], C. Guardasoni[1,+], G. Speroni[3]

[1]Dept. of Mathematical, Physical and Computer Sciences, University of Parma, Italy
[2]Engineering Mathematics, University of Innsbruck, Austria
[3]Dept. of Mathematics, Polytechnic of Milan, Italy
[+]Members of the INdAM-GNCS Research Group, Italy

May 26, 2023

Keywords: Energetic Boundary Element Method, 2D Elastodynamics, Mixed Boundary Problems.

AMS: 65M38, 65M80.

Abstract

In this article we present a boundary element formulation for time dependent elastodynamic wave propagation in 2D interior domains with inhomogeneous boundary conditions. These are imposed in a weak sense, allowing the unified implementation of a wide range of boundary data, from pure Dirichlet to pure Neumann and mixed ones. Numerical experiments indicate that the considered approach is effective and reliable. We discuss several numerical results which, compared to those obtained by the strong imposition of the boundary data, highlight the equivalence in the behavior of the error.

1 Introduction

The weak imposition of boundary conditions is a standard practice in finite element methods. Such approaches do not impose the boundary data exactly, but only in a mesh-dependent way which recovers the exact boundary condition asymptotically [21]. They are particularly useful for mixed boundary value problems, as they allow a unified implementation of different conditions on different parts of the boundary.

For homogeneous problems, boundary element methods (BEMs) provide an efficient alternative to finite element approaches. They rewrite the strong formulation of the problem with mixed boundary conditions as a system of integral equations on the boundary of the domain (BIEs). The resulting numerical schemes require the assembly of the integral operators on subsets of the boundary mesh, depending on the partition of the boundary itself.

For time dependent problems, a detailed exposition of the mathematical background of time domain BIEs and their discretizations is available in the monograph by Sayas [20], including methods based on convolution quadrature. See [12, 15, 17] for more concise introductions.

The current article presents a numerical analysis of a boundary element formulation for time dependent elastodynamic wave propagation in 2D interior domains with inhomogeneous boundary conditions, which are imposed in a weak sense. In spite of the increased number of degrees of freedom, this approach is justified by the flexibility useful in applications such as, for instance, in non-conforming BEM-FEM coupling and for nonlinear boundary conditions. Moreover, it relates to recent advances in the time independent setting [8, 9, 10]: unlike the stabilized methods presented there, we here empirically observe quasi-optimal convergence as well as long-time stability for the proposed, simple formulation.

*Corresponding author: giulia.dicredico@unipr.it

To be specific, in a bounded, Lipschitz domain $\Omega \subset \mathbb{R}^2$ with boundary Γ, we consider the wave propagation in a linearly elastic medium described by the well known Lamé equation, in the unknown displacement field $\mathbf{u}$ in Ω and on the time interval $[0, T]$. Inhomogeneous Dirichlet, Neumann or mixed boundary conditions are taken into account, as indicated in the following Figure 1, where $\mathbf{p}$ denotes the boundary traction, and $\Gamma_{D/N}$ the Dirichlet, respectively Neumann parts of the boundary. For simplicity, homogeneous initial data are assumed (for the setup of integral formulations including inhomogeneous initial conditions in elastodynamic wave propagation problems, the reader may refer to [13]).

The classical time domain boundary integral reformulation for the Lamé problem involves the following BIEs

$$\mathcal{V}\mathbf{p} - (\mathcal{K} + \tfrac{1}{2})\,\mathbf{u} = 0 \tag{1}$$

$$(\mathcal{K}^* - \tfrac{1}{2})\mathbf{p} - \mathcal{W}\mathbf{u} = 0, \tag{2}$$

based on the single layer operator $\mathcal{V}$, the double layer operator $\mathcal{K}$, the adjoint double layer $\mathcal{K}^*$ and the hypersingular integral operator $\mathcal{W}$, with strong imposition of boundary data. In this paper, we address the elastodynamic problem considering only (1), therefore avoiding the coding of $\mathcal{W}$, and imposing the boundary conditions in the following weak sense:

$$\begin{aligned}
&\langle \dot{\mathcal{V}}\mathbf{p}, \phi\rangle_{L^2(\Gamma\times(0,T])} - \langle (\mathcal{K} + \dot{\tfrac{1}{2}})\,\mathbf{u}, \boldsymbol{\phi}\rangle_{L^2(\Gamma\times(0,T])} = 0 \\
&\langle \dot{\mathbf{u}}, \boldsymbol{\psi}\rangle_{L^2(\Gamma_D\times(0,T])} = \langle \dot{\overline{\mathbf{u}}}, \boldsymbol{\psi}\rangle_{L^2(\Gamma_D\times(0,T])} \\
&\langle \mathbf{p}, \dot{\boldsymbol{\psi}}\rangle_{L^2(\Gamma_N\times(0,T])} = \langle \overline{\mathbf{p}}, \dot{\boldsymbol{\psi}}\rangle_{L^2(\Gamma_N\times(0,T])}
\end{aligned} \tag{3}$$

where $\boldsymbol{\phi}$, $\boldsymbol{\psi}$ are suitable test functions, $\overline{\mathbf{u}}, \overline{\mathbf{p}}$ are given boundary data and upper dots denote derivative with respect to time.

In the proposed formulations, we choose the traditional trial and test spaces in the time variable (i.e., H^1 for displacements and L^2 for tractions), but in the space variable we are required to combine them in a non-standard way. The resulting discrete systems are fully coupled.

Numerical experiments show stability under space-time mesh refinements as well as long-time stability for both weak and strong imposition of the boundary conditions and compare the two approaches. Quasi-optimal convergence rates are observed, i.e. with the rate expected for the best approximation of the solution in the space-time L^2 norm. The error of the numerical solutions shows comparable behavior for the different methods.

This paper contributes to our recent progress on BEM for time-dependent problems [1, 2, 3, 4]. It is structured as follows: after the introduction of the model problem with its energetic integral reformulation in Section 2 and the related discretization in Section 3, we address the numerical study of (3) for Dirichlet, Neumann and mixed boundary conditions in Section 4, 5, 6, respectively. Final remarks on long-time stability are briefly discussed in Section 7. Conclusions are drawn in Section 8.

2 Model problem and energetic weak formulation

The main theme of this paper is the coupling of the time-domain Energetic Boundary Element Method (EBEM) with a weak imposition of boundary conditions. We consider the elastodynamic equations in a $2D$ domain with mixed boundary conditions, which prescribe the traction, respectively the displacement on disjoint subsets of the boundary, and trivial initial conditions, as briefly described in the previous Section. This initial-mixed boundary value problem has a solution of low regularity extensively studied because of its numerical challenges.

The evident numerical instabilities appearing in the benchmark problem depicted in Fig. 1, when applying a standard BEM, are taken from [14], where the author suggests they may arise depending on the ratio between time and space discretization parameters. This issue motivated the analysis and development of an unconditionally stable formulation [3, 6]. Here, this example is taken into account as crucial test for the numerical analysis of the stability and accuracy of our implementation of time-domain EBEM applied to 2D elastodynamics.

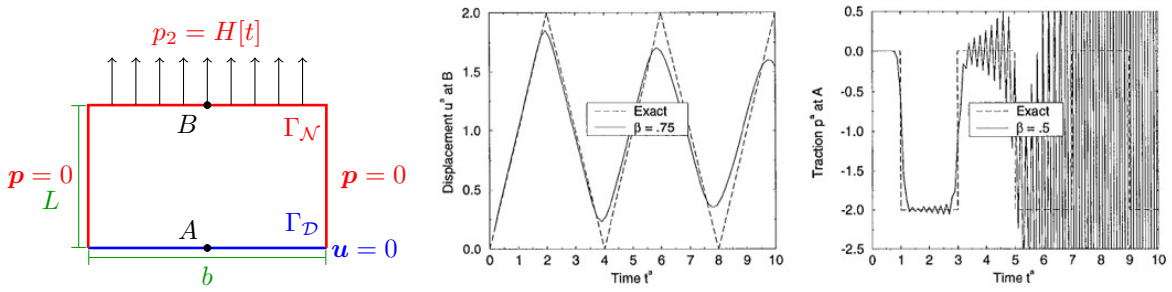

Figure 1: on the left, the reference 2D elastodynamic test problem and, on the right, the time history of the displacement at point B and of the traction at point A affected by instabilities as displayed in [14] with $\beta = c_P \Delta t/\Delta x$.

Given a bounded Lipschitz domain $\Omega \subset \mathbb{R}^2$ with boundary $\Gamma = \Gamma_D \cup \Gamma_N$, representing a linear homogeneous elastic medium, and a bounded time interval $[0, T]$, we consider the differential problem

$$\sum_{h,k,l=1}^{2} \frac{\partial}{\partial x_h}\left(\mathcal{C}_{ih}^{kl}\frac{\partial u_k}{\partial x_l}(\mathbf{x},t)\right) - \rho\ddot{u}_i(\mathbf{x},t) = 0 \quad i = 1,2\,,\ (\mathbf{x},t) \in \Omega \times (0,T] \tag{4}$$

$$\mathbf{u}(\mathbf{x},0) = 0; \quad \dot{\mathbf{u}}(\mathbf{x},0) = 0 \qquad \mathbf{x} \in \Omega \tag{5}$$

$$\mathbf{u}(\mathbf{x},t) = \overline{\mathbf{u}}(\mathbf{x},t) \qquad \mathbf{x} \in \Sigma_D := \Gamma_D \times (0,T] \tag{6}$$

$$\mathbf{p}(\mathbf{x},t) = \overline{\mathbf{p}}(\mathbf{x},t) \qquad \mathbf{x} \in \Sigma_N := \Gamma_N \times (0,T] \tag{7}$$

where ρ is the mass density and $C_{ih}^{k\ell}$ is the Hooke stress tensor, defined by

$$C_{ih}^{k\ell} = \lambda\delta_{ih}\delta_{k\ell} + \mu(\delta_{ik}\delta_{h\ell} + \delta_{i\ell}\delta_{hk})\,, \qquad h,k,\ell = 1,2 \tag{8}$$

with μ the shear modulus and λ the Lamé parameter. If $\mathbf{n}$ denotes the outward unit normal vector to the boundary, the Hooke tensor allows to define the traction vector

$$p_i(\mathbf{x},t) := \sum_{h,k,l=1}^{2} \mathcal{C}_{ih}^{kl}\frac{\partial u_k}{\partial x_l}(\mathbf{x},t)n_h(\mathbf{x}) \quad i = 1,2\,. \tag{9}$$

As it is well known, the displacement $\mathbf{u}(\mathbf{x},t)$ may be decomposed into an irrotational (or dilatational) part $\mathbf{u}_P(\mathbf{x},t)$ and a rotational (or equivoluminal) part $\mathbf{u}_S(\mathbf{x},t)$

$$\mathbf{u} = \mathbf{u}_P + \mathbf{u}_S = \nabla\phi + \nabla \wedge \boldsymbol{\psi} \tag{10}$$

satisfying the scalar and the vector wave equations

$$c_P^2\Delta\phi - \ddot{\phi} = 0$$

$$c_S^2\boldsymbol{\Delta}\boldsymbol{\psi} - \ddot{\boldsymbol{\psi}} = 0$$

propagating with speeds

$$c_P := \sqrt{\frac{\lambda + 2\mu}{\rho}} > \sqrt{\frac{\mu}{\rho}} := c_S \tag{11}$$

giving them the names *primary* and *secondary* waves.
For the elastodynamic equations, assuming null strain in the direction orthogonal to that of stress application and $\lambda = 0$ ($c_P = \sqrt{2}c_S$), the exact solution of the strip problem with mixed boundary conditions as configured in Fig. 1 on the left, traces back to the solution of the corresponding 1D problem with velocity c_P, depending only on the distance $z \in [0, L]$ from the basis of the 1D bar (see Fig. 2 on the left) and on time $t \in [0, T]$. In this case, the displacement is explicitly known and given by the closed-form expression

$$\begin{aligned}\bar{u}(z,t) \;=\; & \frac{H[t]}{\rho c_P^2}\sum_{k=0}^{\lceil c_P T/(2L)\rceil}(-1)^k\left\{\big(c_P t - 2kL - (L-z)\big)H\left[\frac{c_P t - 2kL - (L-z)}{c_P}\right]\right. \\ & - \left.\big(c_P t - 2(k+1)L + (L-z)\big)H\left[\frac{c_P t - 2(k+1)L + (L-z)}{c_P}\right]\right\},\end{aligned} \tag{12}$$

where $H[\cdot]$ is the Heaviside function; the corresponding closed-form expression for the traction at the basis of the 1D bar ($z = 0$) is

$$\bar{p}(0,t) = \frac{H[t]}{\rho c_P^2} \sum_{k=0}^{\lceil c_P T/(2L)\rceil} (-1)^k \left\{ H\left[\frac{c_P t - (2k+1)L}{c_P}\right] - H\left[\frac{c_P t - (2k+3)L}{c_P}\right] \right\}. \tag{13}$$

Some plots of this analytical solution are shown in Fig. 2.
For the 2D benchmark problem taken into account, the exact displacement turns out to be

$$\mathbf{u}(\mathbf{x},t) = \bar{u}(x_2,t)\,[0,1]^\top, \quad (\mathbf{x},t) \in \Omega \times [0,T];$$

hence, in particular on the boundary, we have $\mathbf{u} \in [H^s([0,T];H^s(\Gamma))]^2$ with $s = \frac{3}{2} - \varepsilon$, and $\mathbf{p} \in [H^q([0,T];H^q(\Gamma))]^2$ with $q = \frac{1}{2} - \varepsilon$, for all $\varepsilon > 0$.

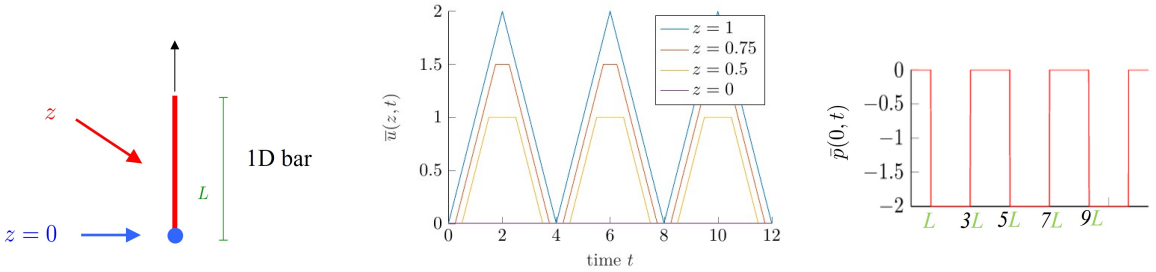

Figure 2: from left to right, the reference 1D test problem, the exact displacement at some height of the rod and the exact traction at the bottom.

The complete integral representation formula for the two components of the solution $\mathbf{u}(\mathbf{x},t)$ of (4) is, for $i = 1, 2$

$$u_i(\mathbf{x},t) = (\mathcal{V}\,\mathbf{p})_i\,(\mathbf{x},t) - (\mathcal{K}\,\mathbf{u})_i\,(\mathbf{x},t), \qquad (\mathbf{x},t) \in \Omega \times (0,T]. \tag{14}$$

It involves the single layer operator

$$(\mathcal{V}\mathbf{p})_i\,(\mathbf{x},t) := \sum_{j=1}^{2} \int_0^t \int_\Gamma G_{ij}(\mathbf{x},\boldsymbol{\xi};t,\tau)\,p_j(\boldsymbol{\xi},\tau) d\Gamma_{\boldsymbol{\xi}} d\tau \tag{15}$$

and the double layer operator

$$(\mathcal{K}\mathbf{u})_i\,(\mathbf{x},t) := \sum_{j=1}^{2} \int_0^t \int_\Gamma \sum_{h,k,l=1}^{2} \mathcal{C}_{jh}^{kl} \frac{\partial G_{ik}}{\partial y_l}(\mathbf{x},\boldsymbol{\xi};t,\tau)\,u_j(\boldsymbol{\xi},\tau) d\Gamma_{\boldsymbol{\xi}} d\tau \tag{16}$$

which are defined in terms of the fundamental solution

$$\begin{aligned} G_{ij}(\mathbf{x},\boldsymbol{\xi};t,\tau) \;:=\; & \frac{H\,[c_P(t-\tau)-r]}{2\pi\rho c_P} \left\{ \frac{r_i\,r_j}{r^4} \frac{2c_P^2(t-\tau)^2 - r^2}{\sqrt{c_P^2(t-\tau)^2 - r^2}} - \frac{\delta_{ij}}{r^2} \sqrt{c_P^2(t-\tau)^2 - r^2} \right\} \\ - \; & \frac{H\,[c_S(t-\tau)-r]}{2\pi\rho c_S} \left\{ \frac{r_i\,r_j}{r^4} \frac{2c_S^2(t-\tau)^2 - r^2}{\sqrt{c_S^2(t-\tau)^2 - r^2}} - \frac{\delta_{ij}}{r^2} \frac{c_S^2(t-\tau)^2}{\sqrt{c_S^2(t-\tau)^2 - r^2}} \right\}. \end{aligned} \tag{17}$$

The vector $\mathbf{r}$ here denotes the difference between the source and field points $\mathbf{x}$ and $\boldsymbol{\xi}$,

$$\mathbf{r} := \mathbf{x} - \boldsymbol{\xi} = (r_1, r_2) = (x_1 - \xi_1, x_2 - \xi_2).$$

Its components are denoted by r_i and its Euclidean norm by $r = |\mathbf{r}| = \sqrt{r_1^2 + r_2^2}$.
The resulting BIEs to be discretized by BEM are, for $i = 1, 2$

$$\frac{1}{2} u_i(\mathbf{x},t) = (\mathcal{V}\,\mathbf{p})_i\,(\mathbf{x},t) - (\mathcal{K}\,\mathbf{u})_i\,(\mathbf{x},t), \qquad (\mathbf{x},t) \in \Sigma := \Gamma \times (0,T], \tag{18}$$

which can be written in matrix form as

$$\frac{1}{2}\begin{pmatrix} u_1(\mathbf{x},t) \\ u_2(\mathbf{x},t) \end{pmatrix} = \begin{pmatrix} \mathcal{V}^{11} & \mathcal{V}^{12} \\ \mathcal{V}^{21} & \mathcal{V}^{22} \end{pmatrix} \begin{pmatrix} p_1(\mathbf{x},t) \\ p_2(\mathbf{x},t) \end{pmatrix} - \begin{pmatrix} \mathcal{K}^{11} & \mathcal{K}^{12} \\ \mathcal{K}^{21} & \mathcal{K}^{22} \end{pmatrix} \begin{pmatrix} u_1(\mathbf{x},t) \\ u_2(\mathbf{x},t) \end{pmatrix}.$$

Moreover, the following energy relation, as proved in Appendix A, holds:

$$\begin{aligned} \mathcal{E}(\mathbf{u},T) &:= \frac{1}{2}\sum_{i=1}^{n}\left\{ \int_\Omega \rho \dot{u}_i^2(\mathrm{x},T)d\mathrm{x} + \int_\Omega \sum_{h,k,l=1}^{n} \mathcal{C}_{ih}^{kl}\frac{\partial u_k}{\partial y_l}(\mathbf{x},T)\frac{\partial u_i}{\partial y_h}(\mathbf{x},T)d\mathbf{x} \right\} \\ &= \sum_{i=1}^{n}\int_0^T \int_\Gamma p_i(\mathbf{x},t)\dot{u}_i(\mathbf{x},t)d\mathbf{x}dt. \end{aligned} \tag{19}$$

The energy relation suggests to introduce a positive space-time bilinear form obtained as the space-time integral of the boundary traction and the time derivative of displacement. Since BIE (18) represents the displacement over the boundary, it is derived w.r.t. time and projected onto the traction functional space, giving the so-called energetic weak formulation of (18) proposed in [4]:

$$\frac{1}{2}\left\langle \dot{u}_i(\mathbf{x},t), \phi_i(\mathbf{x},t) \right\rangle_{L^2(\Sigma)} = \left\langle (\dot{\mathcal{V}}\mathbf{p})_i(\mathbf{x},t), \phi_i(\mathbf{x},t) \right\rangle_{L^2(\Sigma)} - \left\langle (\dot{\mathcal{K}}\mathbf{u})_i(\mathbf{x},t), \phi_i(\mathbf{x},t) \right\rangle_{L^2(\Sigma)} \tag{20}$$

where

$$u_i \in H^1\big([0,T]; H^{\frac{1}{2}}(\Gamma)\big) \qquad p_i, \phi_i \in L^2\big([0,T]; H^{-\frac{1}{2}}(\Gamma)\big), \qquad i = 1,2\,.$$

3 Discretization

Choosing a uniform decomposition of the time interval $[0,T]$ with time step Δt

$$\Delta t = T/N_{\Delta t} \quad N_{\Delta t} \in \mathbb{N}^+, \quad t_n = n\Delta t, \quad n = 0,\dots,N_{\Delta t}\,,$$

the space of continuous piece-wise linear basis functions is denoted by $V_{\Delta t,1}$ with basis

$$r_n(t) := \frac{t-t_n}{\Delta t}H[t-t_n] - \frac{t-t_{n+1}}{\Delta t}H[t-t_{n+1}] \tag{21}$$

and the space of piece-wise constant basis functions can be denoted by $V_{\Delta t,0}$ with basis

$$v_n(t) := H[t-t_n] - H[t-t_{n+1}]\,. \tag{22}$$

We consider for Γ a decomposition of M segments e_i and M nodes $\mathbf{x}_i$, $i = 1,\cdots,M$, such that

$$\Gamma = \bigcup_{i=1}^{M} e_i \qquad e_i \cap e_j = \emptyset,\ i \neq j \qquad \text{length}(e_i) =: \Delta x_i \leq \Delta x\,,$$

equipped with piece-wise polynomial boundary element basis functions of degree d. Denoting by $\mathcal{P}_d$ the space of polynomials of degree d, we consider the following approximation spaces:

$$X^0_{\Delta x,d} := \{w \in C^0(\Gamma) : w_{|e_i} \in \mathcal{P}_d,\ i = 1,\dots,M\}\,, \tag{23}$$

and

$$X^{-1}_{\Delta x,d} := \{w \in L^2(\Gamma) : w_{|e_i} \in \mathcal{P}_d,\ i = 1,\dots,M\}\,. \tag{24}$$

A basis of the approximation space on Γ for the components of the displacement is denoted by $w_m^{\mathbf{u}}$, while $w_m^{\mathbf{p}}$ denotes a basis of the approximation space on Γ for the components of the traction. For this latter, examples referred to $d = 0$ and $d = 1$ are shown in Fig. 3. Then, the components of the displacement $\mathbf{u}$ and the traction $\mathbf{p}$ involved in the energetic weak formulation (20) are approximated by the following linear combinations:

$$u_i(\mathbf{x},t) \approx u_{i,\Delta x,\Delta t}(\mathbf{x},t) = \sum_{n=0}^{N_{\Delta t}-1}\sum_{m=1}^{M_u} \alpha_{nm}^{\mathbf{u},i} w_m^{\mathbf{u}}(\mathbf{x}) r_n(t), \quad i = 1,2, \tag{25}$$

$$p_i(\mathbf{x},t) \approx p_{i,\Delta x,\Delta t}(\mathbf{x},t) = \sum_{n=0}^{N_{\Delta t}-1}\sum_{m=1}^{M_p} \alpha_{nm}^{\mathbf{p},i} w_m^{\mathbf{p}}(\mathbf{x}) v_n(t), \quad i = 1,2. \tag{26}$$

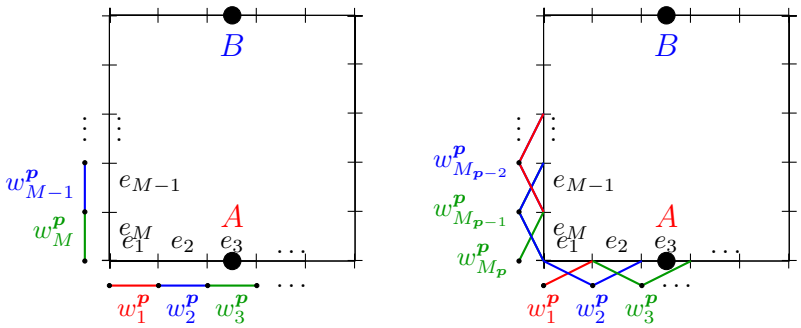

Figure 3: from left to right, piece-wise constant basis functions and piece-wise linear basis functions over the strip boundary for the representation of the components of traction $\mathbf{p}$.

Remark: On a quasi-uniform spatial mesh, with the employed discretization, the best approximation error for an exact solution $\mathbf{u} \in [H^s([0,T]; H^s(\Gamma))]^2$ is $\|\mathbf{u} - \mathbf{u}_{\Delta x,\Delta t}\|_{L^2(\Sigma)} \leq C(\Delta x)^{\min\{s,d+1\}}$, provided Δt is sufficiently small with respect to Δx. Analogous results hold for the best approximation of the traction $\mathbf{p}$.

At the end of the discretization phase, we will have to handle a linear system with unknowns

$$\boldsymbol{\alpha}^{(\ell)} = \begin{pmatrix} \boldsymbol{\alpha}^{\mathbf{p}} \\ \boldsymbol{\alpha}^{\mathbf{u}} \end{pmatrix}^{(\ell)} \in \mathbb{R}^{2M_p+2M_u} \qquad \ell = 0, \ldots, N_{\Delta t-1}\,. \tag{27}$$

and a block lower triangular Toeplitz matrix

$$\mathbb{E} = \begin{pmatrix} \mathbb{E}^{(0)} & 0 & 0 & \cdots & 0 \\ \mathbb{E}^{(1)} & \mathbb{E}^{(0)} & 0 & \cdots & 0 \\ \mathbb{E}^{(2)} & \mathbb{E}^{(1)} & \mathbb{E}^{(0)} & \cdots & 0 \\ \vdots & \vdots & \vdots & \ddots & \vdots \\ \mathbb{E}^{(N_{\Delta t-1})} & \mathbb{E}^{(N_{\Delta t-2})} & \mathbb{E}^{(N_{\Delta t-3})} & \cdots & \mathbb{E}^{(0)} \end{pmatrix}. \tag{28}$$

This particular structure, often put in evidence in previous articles about EBEM (see e.g. [6, 1, 2, 4]), is due to the time independence of constants in the model equation (4) that implies to have a Green function, like that in (17), depending on time only through difference between source and field time instants t and τ.
The entries of the right hand side depend on the assigned boundary data; the entries of the matrix involve integrals, double in time variables and double in space variables: due to the choice of time basis functions, the time integration is performed analytically, while the subsequent numerical integration in space is not trivial and depends on the involved integral operators, as shown in the following.
Assigning $\ell = \tilde{n} - n = 0, \ldots, N_{\Delta t} - 1$ as index of temporal block with $\tilde{n}, n = 0, \ldots, N_{\Delta t} - 1$, $i, j = 1, 2$ as indexes of the vectorial components, $\tilde{m}, m$ as indexes of basis functions in space, the general expression for the matrix terms related to single layer potential (15) is

$$\left(\mathbb{V}^{(\ell)}_{ij}\right)_{\tilde{m}m} = -\sum_{\zeta,\varsigma=0}^{1} \frac{(-1)^{\zeta+\varsigma}}{2\pi\rho} \int_\Gamma \int_\Gamma w^{\mathbf{p}}_{\tilde{m}}(\mathbf{x}) w^{\mathbf{p}}_m(\boldsymbol{\xi}) \nu_{ij}(\mathbf{r}; \Delta_{\tilde{n}+\zeta,n+\varsigma}) d\Gamma_{\boldsymbol{x}} d\Gamma_{\boldsymbol{\xi}} \tag{29}$$

where $\Delta_{\tilde{n}+\zeta,n+\varsigma} = t_{\tilde{n}+\zeta} - t_{n+\varsigma}$,

$$\begin{aligned} \nu_{ij}(\mathbf{r}; \Delta) = &\left(\frac{r_i\, r_j}{r^4} - \frac{\delta_{ij}}{2r^2}\right) \left[\frac{H[c_P\Delta - r]}{c_P} \Delta h_{P,1}(r; \Delta) - \frac{H[c_S\Delta - r]}{c_S} \Delta h_{S,1}(r; \Delta)\right] \\ &+ \frac{\delta_{ij}}{2} \left[\frac{H[c_P\Delta - r]}{c_P^2} h_{P,2}(r; \Delta) + \frac{H[c_S\Delta - r]}{c_S^2} h_{S,2}(r; \Delta)\right] \end{aligned} \tag{30}$$

$$\text{with} \quad h_{\gamma,1}(r; \Delta) = \sqrt{c_\gamma^2\Delta^2 - r^2}, \quad h_{\gamma,2}(r; \Delta) = \log\left(\sqrt{c_\gamma^2\Delta^2 - r^2} + c_\gamma\Delta\right) - \log(r), \quad \gamma = S, P$$

and, the general expression for the matrix terms related to double layer potential (16), is

$$\left(\mathbb{K}_{ij}^{(\ell)}\right)_{\tilde{m}m} = -\sum_{\zeta,\varsigma=0}^{1} \frac{(-1)^{\zeta+\varsigma}}{2\pi\rho\Delta t} \int_{\Gamma}\int_{\Gamma} w_{\tilde{m}}^{\mathbf{p}}(\mathbf{x}) w_{m}^{\mathbf{u}}(\boldsymbol{\xi}) \hat{\nu}_{ij}(\mathbf{r};\Delta_{\tilde{n}+\zeta,n+\varsigma}) d\Gamma_{\boldsymbol{x}} d\Gamma_{\boldsymbol{\xi}} \tag{31}$$

where

$$\begin{aligned}
\hat{\nu}_{ij}(\mathbf{r};\Delta) =& H[c_P\Delta - r]\frac{h_{P,1}(r;\Delta)}{c_P r}\left(\frac{K_P^{ij}}{c_P^2} + \frac{\Delta^2\widetilde{K}_P^{ij}}{r^2}\right) - H[c_S\Delta - r]\frac{h_{S,1}(r;\Delta)}{c_S r}\left(\frac{K_S^{ij}}{c_S^2} + \frac{\Delta^2\widetilde{K}_S^{ij}}{r^2}\right) \qquad (32)\\
K_P^{ij} =& K_P^{ij}(\mathbf{r}) = \frac{1}{r}\left[\left(-\lambda - \frac{2}{3}\mu\right) r_i\, n_j(\boldsymbol{\xi}) - \frac{2}{3}\mu\, r_j\, n_i(\boldsymbol{\xi}) - \frac{2}{3}\mu\,\delta_{ij}\,\mathbf{r}\cdot\mathbf{n}(\boldsymbol{\xi})\right] + \frac{2}{3}\mu\frac{r_i\, r_j\,\mathbf{r}\cdot\mathbf{n}(\boldsymbol{\xi})}{r^3}\\
K_S^{ij} =& K_S^{ij}(\mathbf{r}) = \frac{1}{r}\left[-\frac{2}{3}\mu\, r_i\, n_j(\boldsymbol{\xi}\,) + \frac{1}{3}\mu\, r_j\, n_i(\boldsymbol{\xi}) + \frac{1}{3}\,\mu\,\delta_{ij}\,\mathbf{r}\cdot\mathbf{n}(\boldsymbol{\xi})\right] + \frac{2}{3}\mu\,\frac{r_i\, r_j\,\mathbf{r}\cdot\mathbf{n}(\boldsymbol{\xi})}{r^3}\\
\widetilde{K}_P^{ij} =& \widetilde{K}_P^{ij}(\mathbf{r}) = \frac{1}{r}\left[\frac{2}{3}\mu\, r_i\, n_j(\boldsymbol{\xi}) + \frac{2}{3}\mu\, r_j\, n_i(\boldsymbol{\xi}) + \frac{2}{3}\mu\,\delta_{ij}\,\mathbf{r}\cdot\mathbf{n}(\boldsymbol{\xi})\right] - \frac{8}{3}\mu\,\frac{r_i\, r_j\,\mathbf{r}\cdot\mathbf{n}(\boldsymbol{\xi})}{r^3}\\
\widetilde{K}_S^{ij} =& \widetilde{K}_S^{ij}(\mathbf{r}) = \widetilde{K}_P^{ij}(\mathbf{r}). \qquad (33)
\end{aligned}$$

For $0 \le r \le c_S\Delta$ the single layer kernel ν_{ij} reduces to the form

$$\nu_{ij}(\mathbf{r};\Delta) = \frac{c_P^2 - c_S^2}{c_P c_S}\left(\frac{r_i r_j}{r^2} - \frac{\delta_{ij}}{2}\right)\frac{\Delta}{c_P h_{S,1}(r;\Delta) + c_S h_{P,1}(r;\Delta)} + \frac{\delta_{ij}}{2}\left[\frac{1}{c_P^2}h_{P,2}(r;\Delta) + \frac{1}{c_S^2}h_{S,2}(r;\Delta)\right], \tag{34}$$

while for the double layer kernel it holds

$$\hat{\nu}_{ij}(\mathbf{r};\Delta) = \frac{1}{r}\left(\frac{K_P^{ij}}{c_P^3}h_{P,1}(r;\Delta) - \frac{K_S^{ij}}{c_S^3}h_{S,1}(r;\Delta) + \frac{c_P^2 - c_S^2}{c_P c_S}\frac{\Delta^2\widetilde{K}_P^{ij}}{c_P h_{S,1}(r;\Delta) + c_S h_{P,1}(r;\Delta)}\right). \tag{35}$$

Thanks to these reductions, we deduce that the integrals defining $\left(\mathbb{V}_{ij}^{(\ell)}\right)_{\tilde{m}m}$ and $\left(\mathbb{K}_{ij}^{(\ell)}\right)_{\tilde{m}m}$ are characterized, for $r \to 0$, by a weak singularity $\mathcal{O}(\log(r))$ and a strong singularity $\mathcal{O}(1/r)$, respectively. This compels us to develop ad hoc quadrature strategies for the computation of the above defined integrals: for what concerns those of single layer type, we refer the interested reader to the papers [2, 4, 5], while, in the Appendix B, further details about the techniques adopted for the approximations of the strongly singular integrals (31) are collected.

All the described ingredients are sufficient to discretize the single and double layer operators contribution in (20). Moreover, the weak imposition of mixed boundary conditions (that includes, as particular cases, pure Dirichlet and pure Neumann boundary conditions) is formalized by the addition of dummy equations to the full BIE (20):

Find $\mathbf{u} \in \left[V_{\Delta t,1} \times X^0_{\Delta x,d}\right]^2$ and $\mathbf{p} \in \left[V_{\Delta t,0} \times X^{-1}_{\Delta x,\bar{d}}\right]^2$ *such that*

$$\begin{aligned}
&\left\langle (\dot{\mathcal{V}}\mathbf{p})_i(\mathbf{x},t), \phi_i(\mathbf{x},t)\right\rangle_{L^2(\Sigma)} - \left\langle \left((\mathcal{K} + \dot{\mathcal{I}}/2)\,\mathbf{u}\right)_i(\mathbf{x},t), \phi_i(\mathbf{x},t)\right\rangle_{L^2(\Sigma)} = 0 \quad \forall \boldsymbol{\phi} \in [V_{\Delta t,0} \times X^\star]^2\\
&\left\langle \dot{u}_i(\mathbf{x},t), \psi_i(\mathbf{x},t)\right\rangle_{L^2(\Sigma_D)} = \left\langle \dot{\overline{u}}_i(\mathbf{x},t), \psi_i(\mathbf{x},t)\right\rangle_{L^2(\Sigma_D)} \qquad \forall \boldsymbol{\psi} \in [V_{\Delta t,0} \times X^\star]^2 \qquad (36)\\
&\left\langle p_i(\mathbf{x},t), \dot{\psi}_i(\mathbf{x},t)\right\rangle_{L^2(\Sigma_N)} = \left\langle \overline{p}_i(\mathbf{x},t), \dot{\psi}_i(\mathbf{x},t)\right\rangle_{L^2(\Sigma_N)} \qquad \forall \boldsymbol{\psi} \in [V_{\Delta t,1} \times X^\star]^2
\end{aligned}$$

and, consequently, this directly affects the structure and the dimension of each block $\mathbb{E}^{(\ell)}$ in (28). At this stage, the choice of space test functions X^* has not yet been exercised and it will be matter of numerical analysis in the following sections.

Anyway, let us fix $M_{p,D}$ and $M_{p,N}$ the number of basis functions that represent the traction $\mathbf{p}$ over Γ_D and Γ_N respectively so that $M_p = M_{p,D} + M_{p,N}$ and, analogously for the displacement $\mathbf{u}$, $M_u = M_{u,D} + M_{u,N}$. The resulting linear system of dimension $N_{\Delta t} \times (2M_p + 2M_u)$ has the following structure:

$$\begin{cases} \mathbb{V}\boldsymbol{\alpha}^{\mathbf{p}} & -\left(\mathbb{K} + \frac{1}{2}\mathbb{M}_{\star u}\right)\boldsymbol{\alpha}^{\mathbf{u}} & = \mathbb{O}_{N_{\Delta t} \times 2M_\star} \\ \mathbb{M}_{\star p}\boldsymbol{\alpha}^{\mathbf{p}} & + \mathbb{M}_{\star u}\boldsymbol{\alpha}^{\mathbf{u}} & = \mathbb{M}_{\star p}\widetilde{\mathbf{p}}\big|_{\Gamma_N} + \mathbb{M}_{\star u}\widetilde{\mathbf{u}}\big|_{\Gamma_D} \end{cases}. \tag{37}$$

With a further rearrangement of the unknown coefficients in the following order

$$\boldsymbol{\alpha}^{(\ell)} = \begin{pmatrix} \boldsymbol{\alpha}^{\mathbf{p}}\big|_{\Gamma_D} \\ \boldsymbol{\alpha}^{\mathbf{p}}\big|_{\Gamma_N} \\ \boldsymbol{\alpha}^{\mathbf{u}}\big|_{\Gamma_D} \\ \boldsymbol{\alpha}^{\mathbf{u}}\big|_{\Gamma_N} \end{pmatrix}^{(\ell)} \in \mathbb{R}^{2M_{\mathbf{p},\mathbf{D}}+2M_{\mathbf{p},\mathbf{N}}+2M_{\mathbf{u},\mathbf{D}}+2M_{\mathbf{u},\mathbf{N}}} \qquad \ell = 0, \dots, N_{\Delta t-1}\,,$$

we can define the contribution $\mathbb{V}^{(\ell)}$, $\mathbb{K}^{(\ell)}$, $\mathbb{M}^{(\ell)}_{\star\bullet}$ of (37) to the blocks $\mathbb{E}^{(\ell)}$ in (28). In particular, for the ℓ-th block of mass matrices $\mathbb{M}^{(\ell)}_{\star\bullet}$, with $\star, \bullet = \mathbf{u}, \mathbf{p}$, we have:

$$\begin{bmatrix} \mathbb{M}^{(\ell)}_{\star\bullet} & \mathbb{O}_{M_\star \times M_\bullet} \\ \mathbb{O}_{M_\star \times M_\bullet} & \mathbb{M}^{(\ell)}_{\star\bullet} \end{bmatrix} \quad \text{with entries} \quad \left(\mathbb{M}^{(\ell)}_{\star\bullet}\right)_{\tilde{m}m} = \int_0^T \int_\Gamma w^\star_{\tilde{m}}(\mathbf{x}) w^\bullet_m(\mathbf{x}) v_{\tilde{n}}(t) \dot{r_n}(t) d\Gamma_{\mathbf{x}} dt$$

observing that

$$\begin{aligned} \left(\mathbb{M}^{(0)}_{\star\bullet}\right)_{\tilde{m}m} &= \int_\Gamma w^\star_{\tilde{m}}(\mathbf{x}) w^\bullet_m(\mathbf{x}) d\Gamma_{\mathbf{x}} \\ \left(\mathbb{M}^{(\ell)}_{\star\bullet}\right)_{\tilde{m}m} &= 0 \qquad \ell = 1, \dots, N_{\Delta t-1} \end{aligned} \,. \tag{38}$$

Remark: In the following Sections, we will investigate the approach for the benchmark problem on the strip of Fig. 1, modeled by Eq. (4) for different boundary and null initial conditions (5), $L = b = 1$, $\lambda = 0$, $\rho = 1, c_P = 1, c_S = \frac{1}{\sqrt{2}}$ and, unless otherwise specified, fixing $T = 12$, $\frac{\Delta x}{\Delta t} = c_P$. Moreover, all the following numerical experiments are based on a uniform decomposition of the boundary Γ, obtained setting length$(e_i) = \Delta x$, $i = 1, ..., M$.
Let us finally recall that, from the Remark at the beginning of this section and the regularity of the exact solution given in Section 2, the best approximation of the displacement for piece-wise linear elements converges in $L^2(\Sigma)$ with rate $1.5 - \varepsilon$, for all $\varepsilon > 0$. Analogously the best approximation of the traction, for piecewise constant or piecewise linear elements, converges in $L^2(\Sigma)$ with rate $0.5 - \varepsilon$.

4 Dirichlet Problem

The benchmark problem of Fig. 1 can be interpreted as a Dirichlet-only problem, defining the Dirichlet condition $\overline{\mathbf{u}} = (\overline{u}_1, \overline{u}_2)$ by the imposition of $\bar{u}(z,t)$ in (12) in the vertical direction along the whole boundary $\Gamma \equiv \Gamma_D$ of the strip. Resuming, the Dirichlet boundary condition over the whole boudary is given by

$$\begin{aligned} \overline{u}_1(\mathbf{x}, t) &= 0 \quad (\mathbf{x}, t) \in \Gamma \times (0, T] \\ \overline{u}_2(\mathbf{x}, t) &= \bar{u}(x_2, t) \quad (\mathbf{x}, t) \in \Gamma \times (0, T]\,. \end{aligned} \tag{39}$$

At this point the EBEM can be applied either to the BIEs (18) coming from the complete integral representation formula (14), the so-called direct formulation, or to the BIEs of the indirect formulation based exclusively on the single layer potential (15). The equivalence of these two approaches has already been studied in [4] and in the following we will use only the direct approach, comparing the strong and weak impositions of the datum.

4.1 Strong Imposition of Datum

To approximate the unknown traction $\mathbf{p}$ on the boundary, with a strong imposition of the Dirichlet datum, the EBEM discretization of the weak BIE (20) is rewritten as:

Find $\mathbf{p} \in \left[V_{\Delta t,0} \times X^{-1}_{\Delta x,d}\right]^2$ *such that*

$$\left\langle (\dot{\mathcal{V}}\mathbf{p})_i(\mathbf{x}, t), \phi_i(\mathbf{x}, t) \right\rangle_{L^2(\Sigma)} = \left\langle \left((\mathcal{K} + \dot{\mathcal{I}}/2)\overline{\mathbf{u}}\right)_i(\mathbf{x}, t), \phi_i(\mathbf{x}, t) \right\rangle_{L^2(\Sigma)} \qquad \forall \boldsymbol{\phi} \in \left[V_{\Delta t,0} \times X^{-1}_{\Delta x,\bar{d}}\right]^2 . \tag{40}$$

This first-kind boundary integral equation is weakly coercive and hence well-posed [17]. For more efficient computation, we made the choice of approximating the Dirichlet datum by interpolation, using the already introduced basis functions, i.e.

$$(\overline{\mathbf{u}})_i(\mathbf{x},t) \approx \sum_{n=0}^{N_{\Delta t}-1} \sum_{m=1}^{M_u} \overline{u}^i_{nm} w^{\mathbf{u}}_m(\mathbf{x}) r_n(t) \quad i=1,2\,. \tag{41}$$

In particular, time basis functions $r_n(t) \in V_{\Delta t,1}$ are defined as in (21). Moreover, if $d \geq 1$, $w^{\mathbf{u}}_m(\mathbf{x}) \in X^0_{\Delta x,d}$ and $(\overline{\mathbf{u}})_i(\mathbf{x}_m,t_n) = \overline{u}^i_{nm}$ at the interpolant nodes of the mesh, otherwise, if $d=0$, $w^{\mathbf{u}}_m(\mathbf{x}) \in X^{-1}_{\Delta x,0}$ and $(\overline{\mathbf{u}})_i(\mathbf{x}_m,t_n) = \overline{u}^i_{nm}$ but at $\mathbf{x}_m$ mid-points of the mesh elements. The values $\overline{u}^i_{nm}$ are collected in the vector $\widetilde{\mathbf{u}}$.
In this case $M_p \equiv M_{p,D}$ and $M_u \equiv M_{u,D}$, thus the resulting linear system of dimension $N_{\Delta t} \times 2M_p$ is as follows

$$\mathbb{V}\boldsymbol{\alpha}^{\mathbf{p}} = \left(\mathbb{K} + \frac{1}{2}\mathbb{M}_{pu}\right)\widetilde{\mathbf{u}} \tag{42}$$

where $\boldsymbol{\alpha}^{\mathbf{p}}$ is the vector of the unknowns coefficients in (26), the block lower Toeplitz matrix $\mathbb{E} = \mathbb{V}$ has components defined in (29), the right hand side is a sum of the matrix $\mathbb{K}$ defined in (31) and of the mass matrix $\mathbb{M}_{pu}$ defined in (38).
The following results are obtained by choosing either constant or linear piece-wise defined approximants in space, i.e. $d = \bar{d} = 0$ or $d = \bar{d} = 1$.
The error and the rate of convergence, associated to the discretization parameters $\Delta x = \Delta t$, are defined by components as

$$E^{\Delta x}_i = \|\bar{p}_i - p^{\Delta x}_i\|_{L^2(\Sigma)} \qquad rate^{\Delta x}_i = \log_2\left(\frac{E^{2\Delta x}_i}{E^{\Delta x}_i}\right)\,. \tag{43}$$

Tables 1 and 2 show the errors and the convergence rates for $d = \bar{d} = 0$ and $d = \bar{d} = 1$: the higher polynomial degree for $d = \bar{d} = 1$ leads to improved accuracy. The convergence rates are between 0.50 and 0.75, on the relatively coarse space-time meshes considered.

Traction

Δx	$E^{\Delta x}_1$	$rate^{\Delta x}_1$	$E^{\Delta x}_2$	$rate^{\Delta x}_2$
0.2	0.5347	-	0.4612	-
0.1	0.3705	0.5292	0.3122	0.5630
0.05	0.2574	0.5255	0.2161	0.5306
0.025	0.1793	0.5217	0.1488	0.5388

Table 1: errors and rate of convergence of the traction components along the strip for $d = \bar{d} = 0$.

Traction

Δx	$E^{\Delta x}_1$	$rate^{\Delta x}_1$	$E^{\Delta x}_2$	$rate^{\Delta x}_2$
0.2	0.2567	-	0.3117	-
0.1	0.1465	0.8097	0.1742	0.8392
0.05	0.0930	0.6545	0.1039	0.7454
0.025	0.0608	0.6129	0.0621	0.7439

Table 2: errors and rate of convergence of the traction components along the strip for $d = \bar{d} = 1$.

Also the graphical representation in Fig. 4 of the second component of traction approximation at point A, i.e. in the middle of bottom edge (look at Fig. 3), highlights the improvements achieved refining the mesh with only a very slight presence of Gibbs-like phenomenon usually evident in numerical simulations that reproduce these square waves. The behavior is good for $d = \bar{d} = 0$ and it is even better for $d = \bar{d} = 1$ in Fig. 5.

4.2 Weak Imposition of Datum

With a weak imposition of the datum, the complete energetic weak BIE (20) is coupled with a second weak equation with the dummy unknown $\mathbf{u}$. The resulting EBEM formulation is a particular case of

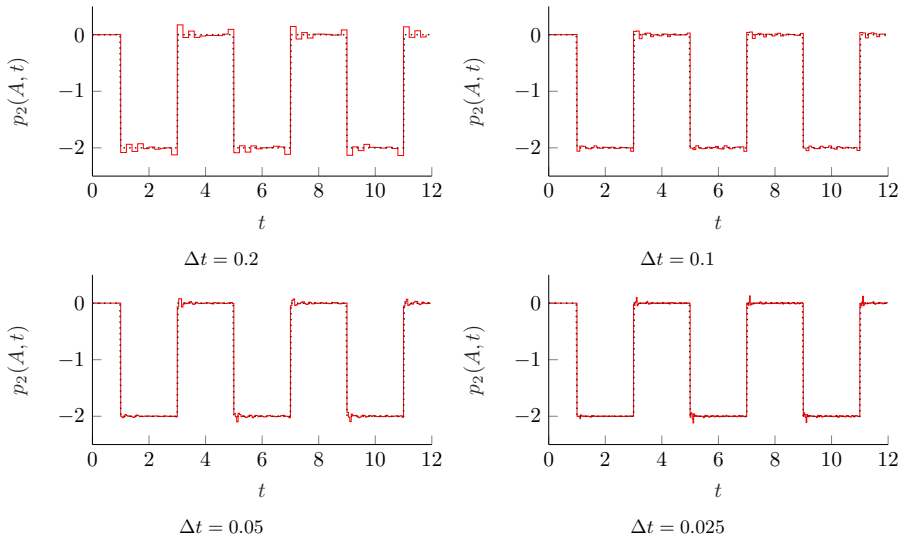

Figure 4: Second component of traction approximation in the middle of bottom edge (point A as depicted in Fig. 3), refining the time-space mesh parameter $\Delta x = \Delta t$, for $d = \bar{d} = 0$.

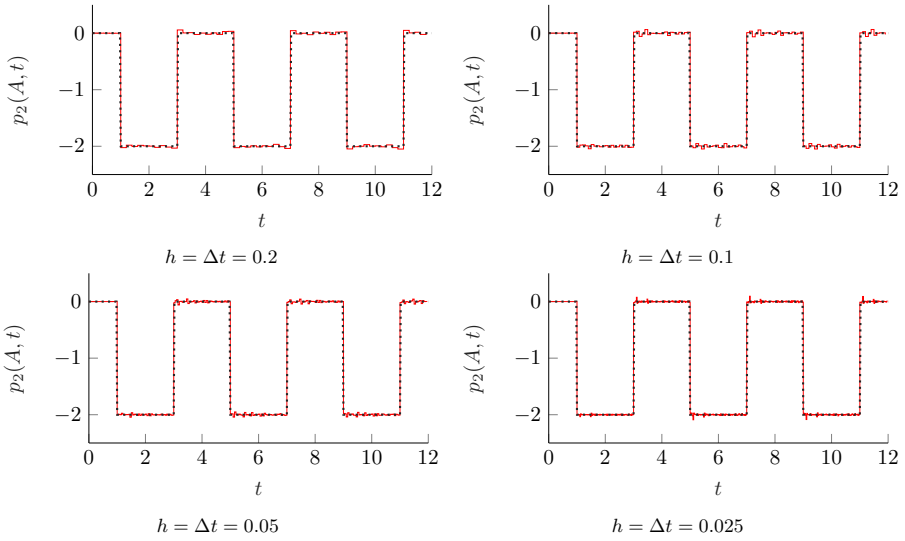

Figure 5: Second component of traction approximation in the middle of bottom edge (point A as depicted in Fig. 3), refining the time-space mesh parameter $\Delta x = \Delta t$, for $d = \bar{d} = 1$.

(36):

$$
\begin{aligned}
&\textit{Find } \mathbf{u} \in \left[V_{\Delta t,1} \times X^{0}_{\Delta x,d}\right]^2 \text{ and } \mathbf{p} \in \left[V_{\Delta t,0} \times X^{-1}_{\Delta x,\bar{d}}\right]^2 \textit{ such that} \\
&\left\langle (\dot{\mathcal{V}}\mathbf{p})_i(\mathbf{x},t), \phi_i(\mathbf{x},t) \right\rangle_{L^2(\Sigma)} - \left\langle \left((\mathcal{K} + \dot{\mathcal{I}}/2)\,\mathbf{u}\right)_i(\mathbf{x},t), \phi_i(\mathbf{x},t) \right\rangle_{L^2(\Sigma)} = 0 \quad \forall \boldsymbol{\phi} \in \left[V_{\Delta t,0} \times X^{-1}_{\Delta x,\bar{d}}\right]^2 \\
&\left\langle \dot{u}_i(\mathbf{x},t), \psi_i(\mathbf{x},t) \right\rangle_{L^2(\Sigma)} = \left\langle \dot{\overline{u}}_i(\mathbf{x},t), \psi_i(\mathbf{x},t) \right\rangle_{L^2(\Sigma)} \qquad \forall \boldsymbol{\psi} \in \left[V_{\Delta t,0} \times X^{0}_{\Delta x,d}\right]^2
\end{aligned}
\tag{44}
$$

where both $\mathbf{u}$ and $\mathbf{p}$ are considered unknowns all over the boundary and so each space of basis functions in space variable, of dimension $2M_u$ and $2M_p$ respectively, is defined on the whole Γ.
In this case, the choice of test functions is due to the need of keeping the Toeplitz matrix blocks squared, i.e.: in each ℓ-th block, the number of columns is determined by the number $2M_p + 2M_u$ of $\mathbf{p}$ and $\mathbf{u}$ unknowns, the number of rows related to the discretization of the weak BIE is the number $2M_p$ of test functions ϕ_i belonging to the traction approximant space and therefore the number of rows related to the weak imposition of the datum must be equal to $2M_u$, forcing the test functions ψ_i to belong to the displacement approximation space, only with regards to the space variable. In Figure 6, the structure of this block-matrix is synthesized.

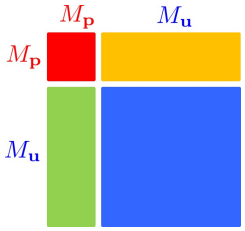

Figure 6: structure of blocks in (44).

Then, with the manipulation (41) of the datum $\overline{\mathbf{u}}$, the resulting linear system is here of dimension $N_{\Delta t} \times (2M_p + 2M_u)$

$$
\begin{cases}
\mathbb{V}\boldsymbol{\alpha}^{\mathbf{p}} - \left(\mathbb{K} + \frac{1}{2}\mathbb{M}_{pu}\right)\boldsymbol{\alpha}^{\mathbf{u}} &= \mathbb{O}_{N_{\Delta t} \times 2M_p} \\
\mathbb{M}_{uu}\boldsymbol{\alpha}^{\mathbf{u}} &= \mathbb{M}_{uu}\widetilde{\mathbf{u}}
\end{cases}
\tag{45}
$$

and with a slight reordering of the rows we can keep the vector $\boldsymbol{\alpha}$ of the unknowns coefficients orderd as in (27) and the matrix structure as in (28). With this strategy, the numerical approximations of traction components, for both choices $d = \bar{d} = 0$ and $d = \bar{d} = 1$, differ 10^{-13} from that obtained in Tables 1 and 2, while the reconstruction of displacement is to floating point accuracy.

5 Neumann Problem

The benchmark problem of Fig. 1 can be defined also as a Neumann-only problem with $\Gamma \equiv \Gamma_N$, applying the Neumann condition $\overline{p}(0,t)$ in (13) at the bottom of the boundary Γ of the strip. Resuming, the Neumann boundary condition $\overline{\mathbf{p}} = (\overline{p}_1, \overline{p}_2)$ is:

$$
\begin{aligned}
&\overline{p}_1(\mathbf{x},t) = 0 \qquad (\mathbf{x},t) \in \Gamma \times (0,T] \\
&\overline{p}_2(\mathbf{x},t) = \begin{cases}
H[t] & (\mathbf{x},t) \in \Gamma \times (0,T] \text{ such that } \mathbf{x} = (x_1, 1) \\
0 & (\mathbf{x},t) \in \Gamma \times (0,T] \text{ such that } \mathbf{x} = (x_1, x_2) \text{ with } 0 < x_2 < 1 \\
\overline{p}(0,t) & (\mathbf{x},t) \in \Gamma \times (0,T] \text{ such that } \mathbf{x} = (x_1, 0)
\end{cases} .
\end{aligned}
\tag{46}
$$

At this point the EBEM can be applied to the BIE (18) coming from the complete integral representation formula (14) (direct formulation) with a strong or a weak impositions of the datum.

5.1 Strong Imposition of Datum

To approximate the unknown displacement $\mathbf{u}$ on the boundary, with a strong imposition of the Neumann datum the EBEM discretization of the weak BIE (20) is rewritten, using traditional test and

trial spaces, as:

$$\textit{Find } \mathbf{u} \in \left[V_{\Delta t,1} \times X^{0}_{\Delta x,d}\right]^2 \textit{ such that}$$

$$\left\langle \left((\mathcal{K} + \dot{\mathcal{I}}/2)\,\mathbf{u}\right)_i(\mathbf{x},t), \phi_i(\mathbf{x},t) \right\rangle_{L^2(\Sigma)} = \left\langle (\dot{\mathcal{V}}\overline{\mathbf{p}})_i(\mathbf{x},t), \phi_i(\mathbf{x},t) \right\rangle_{L^2(\Sigma)} \quad \forall \boldsymbol{\phi} \in \left[V_{\Delta t,0} \times X^{-1}_{\Delta x,\bar{d}}\right]^2 . \tag{47}$$

For the scalar wave equation a similar formulation of the Neumann problem was considered, for example, in [7, 16]. A natural discretization of the direct formulation (47) uses piecewise constant test functions and piecewise linear, continuous trial functions in space for the approximation of $\mathbf{u}$.
With a manipulation of the datum $\overline{\mathbf{p}}$ analogous to that made in (41) for $\overline{\mathbf{u}}$, the resulting linear system is written as

$$\left(\mathbb{K} + \frac{1}{2}\mathbb{M}_{pu}\right)\boldsymbol{\alpha}^{\mathbf{u}} = \mathbb{V}\widetilde{\mathbf{p}}\,. \tag{48}$$

In this case the mass matrix block $\mathbb{M}^{(0)}_{pu}$ associated to the identity operator is singular and the diagonal block $\mathbb{E}^{(0)}$ of the whole matrix $\mathbb{E}$ remains singular also after the addition of matrix $\mathbb{K}$. The same phenomenon is well-known for time-independent boundary integral equations, where sufficient conditions for stable pairs of test and trial spaces have been obtained [11]. Specifically, choosing the same approximation space for test and trial functions leads to a stable discretization for time-independent problems. Therefore, also for the elastodynamic case here taken into account, we have considered the same approximation space for test and trial functions with regards to the space variable: either constant or split at the corners, loosening continuity of the displacement, or continuous on the whole boundary, forcing the test functions to be continuous at the corners.
The sufficiently good numerical results reported in Tables 3 and 4 refer to the formulation

$$\textit{Find } \mathbf{u} \in \left[V_{\Delta t,1} \times X^{-1}_{\Delta x,d}\right]^2 \textit{ such that}$$

$$\left\langle \left((\mathcal{K} + \dot{\mathcal{I}}/2)\,\mathbf{u}\right)_i(\mathbf{x},t), \phi_i(\mathbf{x},t) \right\rangle_{L^2(\Sigma)} = \left\langle (\dot{\mathcal{V}}\overline{\mathbf{p}})_i(\mathbf{x},t), \phi_i(\mathbf{x},t) \right\rangle_{L^2(\Sigma)} \quad \forall \boldsymbol{\phi} \in \left[V_{\Delta t,0} \times X^{-1}_{\Delta x,\bar{d}}\right]^2 , \tag{49}$$

using both piecewise constant and piecewise linear discontinuous basis functions, respectively, on the boundary.

Displacement

Δx	$E_1^{\Delta x}$	$rate_1^{\Delta x}$	$E_2^{\Delta x}$	$rate_2^{\Delta x}$
0.2	0.0736	-	0.0897	-
0.1	0.0303	1.2821	0.0364	1.2293
0.05	0.0107	1.4981	0.0133	1.4494
0.025	0.0038	1.4836	0.0049	1.4406

Table 3: errors and rate of convergence of the discontinuous displacement components along the strip for $d = \bar{d} = 0$.

Displacement

Δx	$E_1^{\Delta x}$	$rate_1^{\Delta x}$	$E_2^{\Delta x}$	$rate_2^{\Delta x}$
0.2	0.0850	-	0.0800	-
0.1	0.0252	1.7523	0.0254	1.6568
0.05	0.0076	1.7330	0.0075	1.7664
0.025	0.0030	1.3215	0.0030	1.3283

Table 4: errors and rate of convergence of the discontinuous displacement components along the strip for $d = \bar{d} = 1$.

Let us observe that the use of piecewise linear basis functions in time and piecewise constant basis

functions in space leads to a convergence rate even better than expected from the Remark at the beginning of Section 3. On the other hand, on the relatively coarse space-time meshes considered, using piecewise linear basis functions in time and space the rate of convergence is not yet stabilized to 1.5. Hence, to confirm this rate of convergence, compatibly with memory resources of the computational devices at our disposal[1], we reduced the final time to $T = 4$ and refined the discretization. The obtained results are collected in Figure 7, which confirms the expected, quasi-optimal convergence rate of 1.5. Figure 7 also shows the condition number of the diagonal block $\mathbb{E}^{(0)}$, the only one to be inverted in the marching-on-in-time solving procedure, which remains bounded as the mesh size tends to 0.

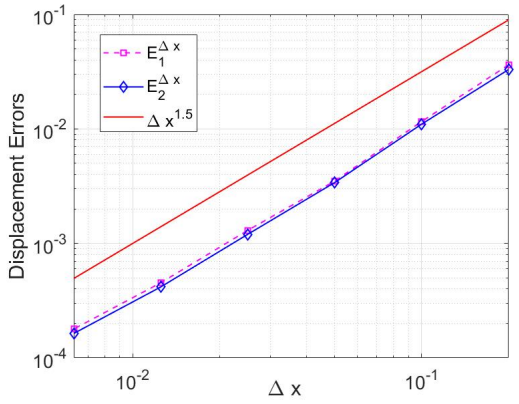

Δx	Cond($\mathbb{E}^{(0)}$)
0.2	9.3578
0.1	9.3880
0.05	9.4555
0.025	9.4776
0.0125	9.4843
0.00625	9.4862

Figure 7: On the left: errors rate of convergence of the discontinuous displacement components along the strip for $d = \bar{d} = 1$ until $T = 4$. On the right: condition number of diagonal block $\mathbb{E}^{(0)}$.

5.2 Weak Imposition of Datum

With a weak imposition of the datum, the complete energetic weak BIE (20) is coupled with a second weak equation for the dummy unknown $\mathbf{p}$. The resulting EBEM formulation (36) collapses into:

$$\begin{aligned} &\textit{Find } \mathbf{u} \in \left[V_{\Delta t,1} \times X^{0}_{\Delta x,d}\right]^2 \text{ and } \mathbf{p} \in \left[V_{\Delta t,0} \times X^{-1}_{\Delta x,\bar{d}}\right]^2 \quad \textit{such that} \\ &\left\langle (\dot{\mathcal{V}}\mathbf{p})_i(\mathbf{x},t), \phi_i(\mathbf{x},t)\right\rangle_{L^2(\Sigma)} - \left\langle \left((\mathcal{K} + \dot{\mathcal{I}}/2)\,\mathbf{u}\right)_i(\mathbf{x},t), \phi_i(\mathbf{x},t)\right\rangle_{L^2(\Sigma)} = 0 \quad \forall \boldsymbol{\phi} \in [V_{\Delta t,0} \times X^{\star}]^2 \\ &\left\langle p_i(\mathbf{x},t), \dot{\psi}_i(\mathbf{x},t)\right\rangle_{L^2(\Sigma)} = \left\langle \overline{p}_i(\mathbf{x},t), \dot{\psi}_i(\mathbf{x},t)\right\rangle_{L^2(\Sigma)} \quad \forall \boldsymbol{\psi} \in [V_{\Delta t,1} \times X^{\star}]^2 \end{aligned} \tag{50}$$

With a manipulation of the datum $\overline{\mathbf{p}}$ analogous to that made in (41) for $\overline{\mathbf{u}}$, the resulting linear system, of dimension $N_{\Delta t} \times (2M_p + 2M_u)$ with $M_p \equiv M_{p,N}$ and $M_u \equiv M_{u,N}$, is here

$$\begin{cases} \mathbb{V}\boldsymbol{\alpha}^{\mathbf{p}} - \left(\mathbb{K} + \frac{1}{2}\mathbb{M}_{\star u}\right)\boldsymbol{\alpha}^{\mathbf{u}} = \mathbb{O}_{N_{\Delta t} \times 2M_\star} \\ \mathbb{M}_{\star p}\boldsymbol{\alpha}^{\mathbf{p}} = \mathbb{M}_{\star p}\widetilde{\mathbf{p}} \end{cases} \tag{51}$$

and, with the usual rearrangement of the rows, we can keep the vector $\boldsymbol{\alpha}$ of the unknown coefficients ordered as in (27) and the matrix structure as in (28).

Since in the matrix blocks, the number of rows must be the same of number of unknowns, we decided to compare two possible choices for test functions space $X^\star$ in (50), starting from the more natural one. In fact, the energy relation (19) suggests to integrate the time-derivative of the displacement by a traction, so the natural space for the test functions in (50) is, in the first equation, the approximant space of tractions and, in the second equation, the approximant space of displacements, i.e.

1. *Find* $\mathbf{u} \in \left[V_{\Delta t,1} \times X^{0}_{\Delta x,d}\right]^2$ and $\mathbf{p} \in \left[V_{\Delta t,0} \times X^{-1}_{\Delta x,\bar{d}}\right]^2$ *such that*

[1] Workstation IEU3HUS, Intel(R)-Xeon(R) processor with CPU ES-2620 0, 12 cores, 2 GHz, 32 Gb RAM.

$$\begin{aligned}
&\left\langle (\dot{\mathcal{V}}\dot{\mathbf{p}})_i(\mathbf{x},t), \phi_i(\mathbf{x},t) \right\rangle_{L^2(\Sigma)} - \left\langle \left((\mathcal{K}+\dot{\mathcal{I}}/2)\,\mathbf{u}\right)_i(\mathbf{x},t), \phi_i(\mathbf{x},t) \right\rangle_{L^2(\Sigma)} = 0 \quad \forall \boldsymbol{\phi} \in \left[V_{\Delta t,0} \times X^{-1}_{\Delta x,\bar{d}}\right]^2 \\
&\left\langle p_i(\mathbf{x},t), \dot{\psi}_i(\mathbf{x},t) \right\rangle_{L^2(\Sigma)} = \left\langle \overline{p}_i(\mathbf{x},t), \dot{\psi}_i(\mathbf{x},t) \right\rangle_{L^2(\Sigma)} \qquad \forall \boldsymbol{\psi} \in \left[V_{\Delta t,1} \times X^{0}_{\Delta x,d}\right]^2
\end{aligned} \tag{52}$$

implying the structure of the blocks synthesized in Fig. 6 and requiring the definition of the ℓ-th block of the matrix $\mathbb{M}_{pu}$ and its transpose $\mathbb{M}_{up}$ by (38) .
This strategy with $d = \bar{d} = 1$ provides displacement errors, shown in Table 5, similar to those shown in Table 4.
The weakly imposed traction boundary datum, unlike in the above experiments, is not reconstructed to floating point accuracy on these coarse meshes, but related numerical results are converging with rate approximately 1, as shown in Table 6.

Displacement

Δx	$E_1^{\Delta x}$	$rate_1^{\Delta x}$	$E_2^{\Delta x}$	$rate_2^{\Delta x}$
0.2	0.0788	-	0.0745	-
0.1	0.0249	1.6627	0.0250	1.5754
0.05	0.0076	1.7049	0.0074	1.7457
0.025	0.0030	1.3268	0.0030	1.3231

Table 5: errors and rate of convergence of the displacement components along the strip for $d = \bar{d} = 1$.

Traction

Δx	$E_1^{\Delta x}$	$rate_1^{\Delta x}$	$E_2^{\Delta x}$	$rate_2^{\Delta x}$
0.2	0.1662	-	0.2409	-
0.1	0.0776	1.0982	0.0934	1.3676
0.05	0.0445	0.8021	0.0531	0.8130
0.025	0.0234	0.9282	0.0266	0.9990

Table 6: reconstruction errors and rate of convergence of the traction components along the strip for $d = \bar{d} = 1$.

Remark: The choice $d = 1$ and $\bar{d} = 0$ is not admissible because the related mass matrix block $\mathbb{M}_{up}^{(0)}$ becomes in this case singular, as already discussed in the case of linear system (48).

An alternative choice for the formulation is given by

2. *Find* $\mathbf{u} \in \left[V_{\Delta t,1} \times X^{0}_{\Delta x,d}\right]^2$ and $\mathbf{p} \in \left[V_{\Delta t,0} \times X^{-1}_{\Delta x,\bar{d}}\right]^2$ *such that*

$$\begin{aligned}
&\left\langle (\dot{\mathcal{V}}\dot{\mathbf{p}})_i(\mathbf{x},t), \phi_i(\mathbf{x},t) \right\rangle_{L^2(\Sigma)} - \left\langle \left((\mathcal{K}+\dot{\mathcal{I}}/2)\,\mathbf{u}\right)_i(\mathbf{x},t), \phi_i(\mathbf{x},t) \right\rangle_{L^2(\Sigma)} = 0 \quad \forall \boldsymbol{\phi} \in \left[V_{\Delta t,0} \times X^{0}_{\Delta x,d}\right]^2 \\
&\left\langle p_i(\mathbf{x},t), \dot{\psi}_i(\mathbf{x},t) \right\rangle_{L^2(\Sigma)} = \left\langle \overline{p}_i(\mathbf{x},t), \dot{\psi}_i(\mathbf{x},t) \right\rangle_{L^2(\Sigma)} \qquad \forall \boldsymbol{\psi} \in \left[V_{\Delta t,1} \times X^{-1}_{\Delta x,\bar{d}}\right]^2
\end{aligned} \tag{53}$$

implying the structure of the blocks synthesized in Fig. 8 and requiring the definition of the ℓ-th block of the matrices $\mathbb{M}_{uu}$ and $\mathbb{M}_{pp}$ by (38).

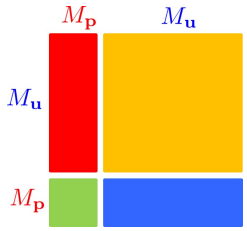

Figure 8: structure of blocks in (53).

In Table 7, obtained fixing $d = \bar{d} = 1$, we observe that the error on the displacement is analogous to that shown in Table 5. It is interesting to note that the reconstruction of the traction boundary datum is here achieved to floating point accuracy, differently from what was reported in Table 6.

Displacement

Δx	$E_1^{\Delta x}$	$rate_1^{\Delta x}$	$E_2^{\Delta x}$	$rate_2^{\Delta x}$
0.2	0.0850	-	0.0800	-
0.1	0.0252	1.7523	0.0254	1.6568
0.05	0.0076	1.7330	0.0075	1.7664
0.025	0.0030	1.3215	0.0030	1.3283

Table 7: errors and rate of convergence of the displacement components along the strip for $d = \bar{d} = 1$.

Another setting is given by renouncing, with regards to the space variable, to continuity of displacement at the corners of the strip, considering the formulation:

3. *Find* $\mathbf{u} \in \left[V_{\Delta t,1} \times X^{-1}_{\Delta x,d}\right]^2$ and $\mathbf{p} \in \left[V_{\Delta t,0} \times X^{-1}_{\Delta x,\bar{d}}\right]^2$ *such that*

$$\begin{aligned} &\left\langle (\dot{\mathcal{V}}\,\mathbf{p})_i(\mathbf{x},t), \phi_i(\mathbf{x},t) \right\rangle_{L^2(\Sigma)} - \left\langle \left((\mathcal{K} + \dot{\mathcal{I}}/2)\,\mathbf{u}\right)_i(\mathbf{x},t), \phi_i(\mathbf{x},t) \right\rangle_{L^2(\Sigma)} = 0 \quad \forall \boldsymbol{\phi} \in \left[V_{\Delta t,0} \times X^{-1}_{\Delta x,d}\right]^2 \\ &\left\langle p_i(\mathbf{x},t), \dot{\psi}_i(\mathbf{x},t) \right\rangle_{L^2(\Sigma)} = \left\langle \overline{p}_i(\mathbf{x},t), \dot{\psi}_i(\mathbf{x},t) \right\rangle_{L^2(\Sigma)} \qquad \forall \boldsymbol{\psi} \in \left[V_{\Delta t,1} \times X^{-1}_{\Delta x,\bar{d}}\right]^2 \end{aligned} \tag{54}$$

With the choice $d = \bar{d} = 0$ the simulations give numerical results shown in Table 8, similar to those obtained by the strong imposition of boundary datum, and again the traction is reconstructed to floating point accuracy.

Displacement

Δx	$E_1^{\Delta x}$	$rate_1^{\Delta x}$	$E_2^{\Delta x}$	$rate_2^{\Delta x}$
0.2	0.0736	-	0.0897	-
0.1	0.0303	1.2821	0.0364	1.2993
0.05	0.0107	1.4981	0.0133	1.4494
0.025	0.0038	1.4836	0.0049	1.4406

Table 8: errors and rate of convergence of the discontinuous displacement components along the strip for $d = \bar{d} = 0$.

With the choice $d = \bar{d} = 1$, the obtained numerical results shown in Table 9 are analogous to the previous ones reported in Tables 5 and 7.

Displacement

Δx	$E_1^{\Delta x}$	$rate_1^{\Delta x}$	$E_2^{\Delta x}$	$rate_2^{\Delta x}$
0.2	0.0817	-	0.0773	-
0.1	0.0256	1.6742	0.0256	1.5943
0.05	0.0077	1.7332	0.0076	1.7521
0.025	0.0030	1.3599	0.0029	1.3899

Table 9: errors and rate of convergence of the discontinuous displacement components along the strip for $d = \bar{d} = 1$.

To confirm the rate of convergence, like for the earlier experiments with $d = \bar{d} = 1$ we reduced the final time to $T = 4$ and refined the discretization. The obtained results are collected in Figure 9, which confirms the expected, quasi-optimal convergence rate of 1.5. Figure 9 also shows the condition number of the diagonal block $\mathbb{E}^{(0)}$. As in the case of strong imposition of the boundary datum the condition number remains bounded as the mesh size tends to 0.

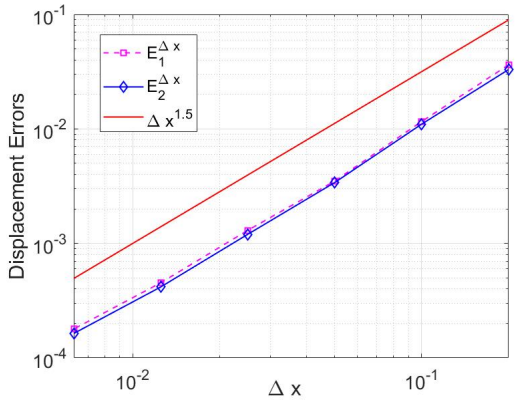

Δx	Cond($\mathbb{E}^{(0)}$)
0.2	17.792
0.1	18.003
0.05	18.131
0.025	18.167
0.0125	18.176
0.00625	18.179

Figure 9: On the left: errors rate of convergence of the discontinuous displacement components along the strip for $d = \bar{d} = 1$ until $T = 4$. On the right: condition number of diagonal block $\mathbb{E}^{(0)}$.

6 Mixed problem

The original configuration of the benchmark problem of Fig. 1 is related to the assignment of mixed boundary conditions, applied on the border of the strip $\Gamma = \Gamma_D \bigcup \Gamma_N$ which is subdivided in Γ_D, equipped with Dirichlet boundary condition, and Γ_N, equipped with Neumann boundary condition, defined by :

$$\begin{aligned} &\overline{\mathbf{u}} = 0 \qquad (\mathbf{x}, t) \in \Gamma \times (0, T] \text{ such that } \mathbf{x} = (x_1, 0) \\ &\overline{\mathbf{p}}(\mathbf{x}, t) = \begin{cases} (0, H[t]) & (\mathbf{x}, t) \in \Gamma \times (0, T] \text{ such that } \mathbf{x} = (x_1, 1) \\ \mathbf{0} & (\mathbf{x}, t) \in \Gamma \times (0, T] \text{ such that } \mathbf{x} = (x_1, x_2) \text{ with } 0 < x_2 < 1 \end{cases} . \end{aligned} \tag{55}$$

At this point the EBEM can be applied to the BIE (18) coming from the complete integral representation formula (14) (direct formulation) with a strong or a weak impositions of the datum.

6.1 Strong Imposition of Datum

To be able to solve the mixed problem with a strong imposition of the datum avoiding the coding of the hypersingular operator $\mathcal{W}$ (see (2)), we are forced to renounce to continuity of displacement in space variable (as in formulation (49) for Neumann problems), splitting all trial and test functions at the corners of Γ and solving, with obvious meaning of notation for discrete functional spaces on subsets of Γ:

$$\textit{Find } \mathbf{u} \in \left[V_{\Delta t,1} \times X^{-1}_{\Delta x,d}(\Gamma_N)\right]^2 \text{ and } \mathbf{p} \in \left[V_{\Delta t,0} \times X^{-1}_{\Delta x,\bar{d}}(\Gamma_D)\right]^2 \textit{ such that, } \forall \boldsymbol{\phi} \in \left[V_{\Delta t,0} \times X^{-1}_{\Delta x,\bar{d}}\right]^2$$

$$\left\langle \left(\mathcal{V}\,\mathbf{p} - (\dot{\mathcal{K}} + \mathcal{I}/2)\,\mathbf{u}\right)_i(\mathbf{x},t), \phi_i(\mathbf{x},t)\right\rangle_{L^2(\Sigma)} = -\left\langle \left(\mathcal{V}\,\overline{\mathbf{p}} - (\dot{\mathcal{K}} + \mathcal{I}/2)\,\overline{\mathbf{u}}\right)_i(\mathbf{x},t), \phi_i(\mathbf{x},t)\right\rangle_{L^2(\Sigma)}. \quad (56)$$

In this situation, the columns of matrices $\mathbb{V}$ and $-(\mathbb{K} + \frac{1}{2}\mathbb{M}_{pu})$ corresponding to the data are moved to the right-hand side. Defining $M_{p,D}$ the number of basis functions that represents each component of the unknown traction $\mathbf{p}$ over Γ_D and defining $M_{u,N}$ the number of basis functions that represents each component of the unknown displacement $\mathbf{u}$ over Γ_N, the resulting linear system is of order $N_{\Delta t} \times (2M_{p,D} + 2M_{u,N})$.
Numerical results reported in Tables 10 and 11 are obtained with $d = \bar{d} = 1$.

Displacement

Δx	$E_1^{\Delta x}$	$rate_1^{\Delta x}$	$E_2^{\Delta x}$	$rate_2^{\Delta x}$
0.2	0.0543	-	0.1247	-
0.1	0.0186	1.5431	0.0339	1.8792
0.05	0.0071	1.3971	0.0105	1.6867
0.025	0.0026	1.4549	0.0036	1.5588

Table 10: errors and rate of convergence of the discontinuous displacement components along the strip for $d = \bar{d} = 1$.

Traction

Δx	$E_1^{\Delta x}$	$rate_1^{\Delta x}$	$E_2^{\Delta x}$	$rate_2^{\Delta x}$
0.2	0.1005	-	0.3866	-
0.1	0.0585	0.7816	0.2076	0.8968
0.05	0.0357	0.7126	0.1254	0.7272
0.025	0.0228	0.6474	0.0768	0.7068

Table 11: errors and rate of convergence of the traction components along the strip for $d = \bar{d} = 1$.

To confirm the rate of convergence, we reduce the final time to $T = 4$ and refined the discretization as done for the Neumann problem: Figure 10 plots the numerical error of the displacements, resp. tractions on the left. The expected, quasi-optimal convergence rates of 1.5 for the displacement and of 0.5 for the traction are observed, even if, differently from the Neumann case, the condition number of diagonal block $\mathbb{E}^{(0)}$, reported on the right, increases like $(\Delta x)^{-1}$.

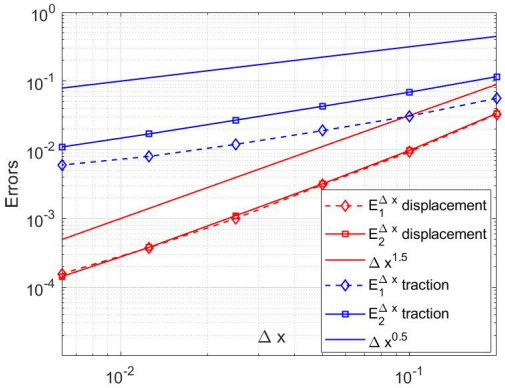

Δx	Cond($\mathbb{E}^{(0)}$)
0.2	3.4861 10^1
0.1	6.7485 10^1
0.05	1.3540 10^2
0.025	2.7146 10^2
0.0125	5.4330 10^2
0.00625	1.0868 10^3

Figure 10: On the left: errors rate of convergence of the discontinuous displacement and traction components along the strip for $d = \bar{d} = 1$ until $T = 4$. On the right: condition number of diagonal block $\mathbb{E}^{(0)}$.

6.2 Weak imposition of the datum

The same problem with weak imposition of the datum can be easily dealt with EBEM starting from formulation (36). We can define $M_{p,D}$ and $M_{p,N}$ the number of basis functions that represents each component of the traction $\mathbf{p}$ over Γ_D and Γ_N respectively so that $M_p = M_{p,D} + M_{p,N}$ and, analogously for the displacement $\mathbf{u}$, $M_u = M_{u,D} + M_{u,N}$. Therefore, the resulting linear system (37) is of dimension $N_{\Delta t} \times (2M_p + 2M_u)$. Similarly as in Section 5.2, we decided to compare two possible choices for test functions space $X^\star$ in (36), starting from the more natural one:

1. *Find* $\mathbf{u} \in \left[V_{\Delta t,1} \times X^0_{\Delta x,d}\right]^2$ *and* $\mathbf{p} \in \left[V_{\Delta t,0} \times X^{-1}_{\Delta x,\bar{d}}\right]^2$ such that

$$\begin{aligned}
&\left\langle (\dot{\mathcal{V}}\mathbf{p})_i(\mathbf{x},t), \phi_i(\mathbf{x},t)\right\rangle_{L^2(\Sigma)} - \left\langle \left((\mathcal{K} + \dot{\mathcal{I}}/2)\,\mathbf{u}\right)_i(\mathbf{x},t), \phi_i(\mathbf{x},t)\right\rangle_{L^2(\Sigma)} = 0 \quad && \forall \boldsymbol{\phi} \in \left[V_{\Delta t,0} \times X^{-1}_{\Delta x,\bar{d}}\right]^2 \\
&\left\langle \dot{u}_i(\mathbf{x},t), \psi_i(\mathbf{x},t)\right\rangle_{L^2(\Sigma_D)} = \left\langle \dot{\bar{u}}_i(\mathbf{x},t), \psi_i(\mathbf{x},t)\right\rangle_{L^2(\Sigma_D)} && \forall \boldsymbol{\psi} \in \left[V_{\Delta t,0} \times X^0_{\Delta x,d}\right]^2 \\
&\left\langle p_i(\mathbf{x},t), \dot{\psi}_i(\mathbf{x},t)\right\rangle_{L^2(\Sigma_N)} = \left\langle \bar{p}_i(\mathbf{x},t), \dot{\psi}_i(\mathbf{x},t)\right\rangle_{L^2(\Sigma_N)} && \forall \boldsymbol{\psi} \in \left[V_{\Delta t,1} \times X^0_{\Delta x,d}\right]^2
\end{aligned} \tag{57}$$

This first choice implies the structure of the blocks synthesized in Fig. 6.
With $d = \bar{d} = 1$, the achieved errors for the global displacement shown in Table 12 and for the global traction displayed in Table 13 are in accordance with those obtained for the displacement in Table 5 and for traction in Table 2.

Displacement

Δx	$E_1^{\Delta x}$	$rate_1^{\Delta x}$	$E_2^{\Delta x}$	$rate_2^{\Delta x}$
0.2	0.0676	-	0.1673	-
0.1	0.0213	1.6696	0.0400	2.0648
0.05	0.0081	1.3963	0.0126	1.6612
0.025	0.0030	1.4509	0.0041	1.6235

Table 12: errors and rate of convergence of the displacement components along the strip for $d = \bar{d} = 1$.

Traction

Δx	$E_1^{\Delta x}$	$rate_1^{\Delta x}$	$E_2^{\Delta x}$	$rate_2^{\Delta x}$
0.2	0.2083	-	0.6290	-
0.1	0.0996	1.0649	0.2606	1.2711
0.05	0.0571	0.8029	0.1701	0.6153
0.025	0.0338	0.7542	0.0949	0.8420

Table 13: errors and rate of convergence of the traction components along the strip for $d = \bar{d} = 1$.

An alternative choice is given by

2. *Find* $\mathbf{u} \in \left[V_{\Delta t,1} \times X^0_{\Delta x,d}\right]^2$ *and* $\mathbf{p} \in \left[V_{\Delta t,0} \times X^{-1}_{\Delta x,\bar{d}}\right]^2$ *such that*

$$\begin{aligned}
&\left\langle (\dot{\mathcal{V}}\mathbf{p})_i(\mathbf{x},t), \phi_i(\mathbf{x},t)\right\rangle_{L^2(\Sigma)} - \left\langle \left((\mathcal{K} + \dot{\mathcal{I}}/2)\,\mathbf{u}\right)_i(\mathbf{x},t), \phi_i(\mathbf{x},t)\right\rangle_{L^2(\Sigma)} = 0 \quad && \forall \boldsymbol{\phi} \in \left[V_{\Delta t,0} \times X^0_{\Delta x,d}\right]^2 \\
&\left\langle \dot{u}_i(\mathbf{x},t), \psi_i(\mathbf{x},t)\right\rangle_{L^2(\Sigma_D)} = \left\langle \dot{\bar{u}}_i(\mathbf{x},t), \psi_i(\mathbf{x},t)\right\rangle_{L^2(\Sigma_D)} && \forall \boldsymbol{\psi} \in \left[V_{\Delta t,0} \times X^{-1}_{\Delta x,\bar{d}}\right]^2 \\
&\left\langle p_i(\mathbf{x},t), \dot{\psi}_i(\mathbf{x},t)\right\rangle_{L^2(\Sigma_N)} = \left\langle \bar{p}_i(\mathbf{x},t), \dot{\psi}_i(\mathbf{x},t)\right\rangle_{L^2(\Sigma_N)} && \forall \boldsymbol{\psi} \in \left[V_{\Delta t,1} \times X^{-1}_{\Delta x,\bar{d}}\right]^2
\end{aligned} \tag{58}$$

that produces blocks with structure synthesized in Fig. 8 and gives a slightly better accuracy than the previous choice for both traction and displacement (look at Tables 14 and 15). In Figs. 11 and 12 the behaviour of displacements and tractions, respectively, is shown refining the discretization parameters.

Displacement

Δx	$E_1^{\Delta x}$	$rate_1^{\Delta x}$	$E_2^{\Delta x}$	$rate_2^{\Delta x}$
0.2	0.0542	-	0.1223	-
0.1	0.0185	1.5505	0.0333	1.8783
0.05	0.0070	1.3984	0.0104	1.6839
0.025	0.0026	1.4548	0.0035	1.5518

Table 14: errors and rate of convergence of the displacement components along the strip for $d = \bar{d} = 1$.

Traction

Δx	$E_1^{\Delta x}$	$rate_1^{\Delta x}$	$E_2^{\Delta x}$	$rate_2^{\Delta x}$
0.2	0.1195	-	0.3623	-
0.1	0.0662	0.8521	0.1989	0.8650
0.05	0.0378	0.8084	0.1215	0.7113
0.025	0.0238	0.6661	0.0751	0.6933

Table 15: errors and rate of convergence of the traction components along the strip for $d = \bar{d} = 1$.

Another setting is given by renouncing, with regards to space variable, to continuity of displacement at the corners of the strip, considering the formulation:

3. *Find* $\mathbf{u} \in \left[V_{\Delta t,1} \times X^{-1}_{\Delta x,1}\right]^2$ *and* $\mathbf{p} \in \left[V_{\Delta t,0} \times X^{-1}_{\Delta x,\bar{d}}\right]^2$ *such that*

$$\begin{aligned}
&\left\langle (\dot{\mathcal{V}}\mathbf{p})_i(\mathbf{x},t), \phi_i(\mathbf{x},t)\right\rangle_{L^2(\Sigma)} - \left\langle \left((\mathcal{K} + \dot{\mathcal{I}}/2)\,\mathbf{u}\right)_i(\mathbf{x},t), \phi_i(\mathbf{x},t)\right\rangle_{L^2(\Sigma)} = 0 \quad \forall \boldsymbol{\phi} \in \left[V_{\Delta t,0} \times X^{-1}_{\Delta x,d}\right]^2 \\
&\left\langle \dot{u}_i(\mathbf{x},t), \psi_i(\mathbf{x},t)\right\rangle_{L^2(\Sigma_D)} = \left\langle \dot{\bar{u}}_i(\mathbf{x},t), \psi_i(\mathbf{x},t)\right\rangle_{L^2(\Sigma_D)} \quad \forall \boldsymbol{\psi} \in \left[V_{\Delta t,0} \times X^{-1}_{\Delta x,\bar{d}}\right]^2 \\
&\left\langle p_i(\mathbf{x},t), \dot{\psi}_i(\mathbf{x},t)\right\rangle_{L^2(\Sigma_N)} = \left\langle \dot{\bar{p}}_i(\mathbf{x},t), \dot{\psi}_i(\mathbf{x},t)\right\rangle_{L^2(\Sigma_N)} \quad \forall \boldsymbol{\psi} \in \left[V_{\Delta t,1} \times X^{-1}_{\Delta x,\bar{d}}\right]^2
\end{aligned} \tag{59}$$

The related simulations give good numerical results, analogous to the previous ones: those obtained fixing $d = \bar{d} = 1$ are collected in Tables 16 and 17.

Displacement

Δx	$E_1^{\Delta x}$	$rate_1^{\Delta x}$	$E_2^{\Delta x}$	$rate_2^{\Delta x}$
0.2	0.0545	-	0.1251	-
0.1	0.0187	1.5449	0.0340	1.8811
0.05	0.0071	1.3990	0.0105	1.6869
0.025	0.0026	1.4557	0.0036	1.5597

Table 16: errors and rate of convergence of the discontinuous displacement components along the strip for $d = \bar{d} = 1$.

Traction

Δx	$E_1^{\Delta x}$	$rate_1^{\Delta x}$	$E_2^{\Delta x}$	$rate_2^{\Delta x}$
0.2	0.1005	-	0.3866	-
0.1	0.0585	0.7816	0.2076	0.8968
0.05	0.0357	0.7126	0.1254	0.7273
0.025	0.0228	0.6474	0.0768	0.7067

Table 17: errors and rate of convergence of the traction components along the strip for $d = \bar{d} = 1$.

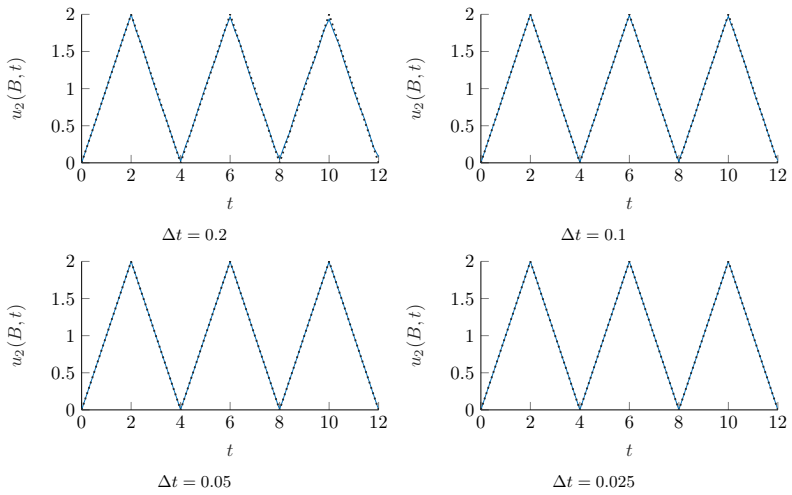

Figure 11: Second component of displacement approximation in the middle of top edge (point B as depicted in Fig. 3), refining the time-space mesh parameter $\Delta x = \Delta t$, for $d = \bar{d} = 1$, with the formulation (58).

To confirm the rate of convergence, we reduce the final time to $T = 4$ and refined the discretization as done for the Neumann problem: Figure 13 plots the numerical error of the displacements, resp. tractions on the left. As for the strong imposition of the boundary conditions, the expected, quasi-optimal convergence rates of 1.5 for the displacement and of 0.5 for the traction are observed, even if, differently from the Neumann case, the condition number of diagonal block $\mathbb{E}^{(0)}$, reported on the right, increases like $(\Delta x)^{-1}$.

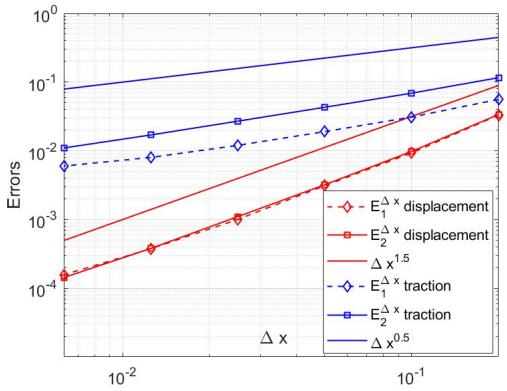

Δx	Cond($\mathbb{E}^{(0)}$)
0.2	9.6483 10^1
0.1	1.9840 10^2
0.05	4.0062 10^2
0.025	8.0330 10^2
0.0125	1.6077 10^3
0.00625	3.2159 10^3

Figure 13: On the left: errors rate of convergence of the discontinuous displacement and traction components along the strip for $d = \bar{d} = 1$ until $T = 4$. On the right: condition number of diagonal block $\mathbb{E}^{(0)}$.

7 Remarks on long-time stability

We finally address the long-time stability of the proposed formulations. We consider in particular the Neumann and mixed problems as solved numerically in the previous Sections, both with weak and strong imposition of the boundary data.

For the Neumann problem we fix $\Delta x = 0.2$, $\Delta t = 0.1$. This coarse mesh corresponds to discretization parameters with ratio $\beta = 0.5$, which gave rise to the explosive instability highlighted from [14] at the beginning of this paper (Figure 1). In Figure 14 we show the vertical component of the displacement at the top side midpoint B of the strip until the very long final time $T = 288$, obtained using the

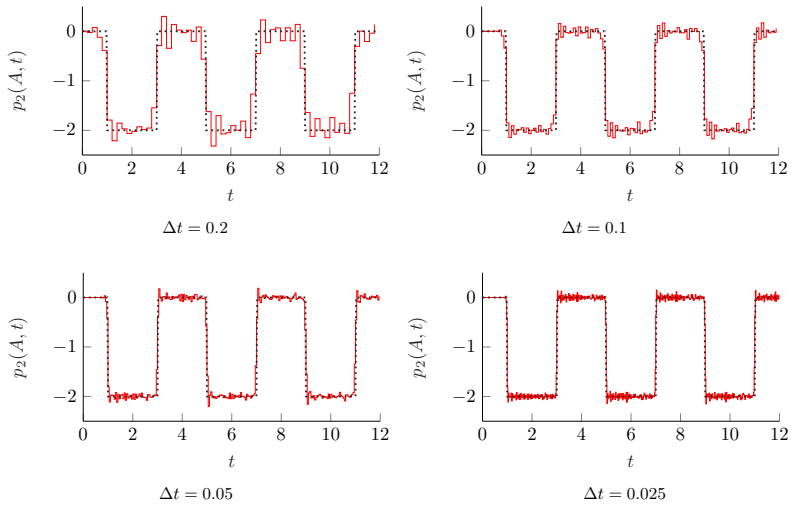

Figure 12: Second component of traction approximation in the middle of bottom edge (point A as depicted in Fig. 3), refining the time-space mesh parameter $\Delta x = \Delta t$, for $d = \bar{d} = 1$, with the formulation (58).

formulation (54) with weak imposition of the boundary datum and $d = \bar{d} = 1$. As one can see, the analytical solution is perfectly recovered and stable. Analogous qualitative results are obtained using the formulation (49) with strong imposition of the boundary datum.
In the more difficult case of mixed boundary conditions, for the same discretization parameters as before, we show in Figures 15 and 16 the vertical displacement at B and the vertical traction at the midpoint A on the bottom of the strip, respectively. The results are obtained using the formulation (59) with weak imposition of the boundary data. Analogous qualitative results have been obtained using the formulation (56), with strong imposition of the boundary condition. The coarse discretization produces in this case a numerical dissipation not present in the Neumann problem results. This can be justified observing that the jumps in time of the traction, given in exact way on the bottom side of the domain boundary in the Neumann problem, are here approximated. The well known Gibbs phenomenon produces a poor approximation of the recovered traction which deteriorates also the approximation of the displacement. While the size of the error is increased with respect to the previous case, the numerical solution remains anyway stable. This gives numerical evidence of the long-time stability of the proposed formulations.

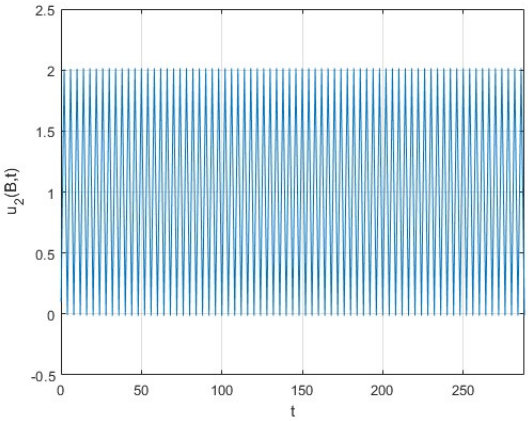

Figure 14: Displacement until time $T = 288$ obtained by formulation (54) with $\Delta x = 0.2$, $\Delta t = 0.1$ and $d = \bar{d} = 1$.

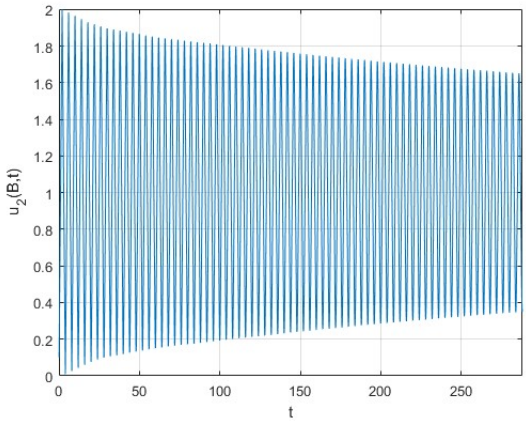

Figure 15: Displacement until time $T = 288$ obtained by formulation (59) with $\Delta x = 0.2$, $\Delta t = 0.1$ and $d = \bar{d} = 1$.

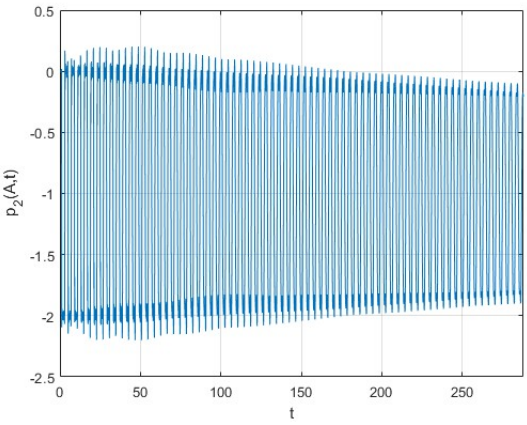

Figure 16: Traction until time $T = 288$ obtained by formulation (59) with $\Delta x = 0.2$, $\Delta t = 0.1$ and $d = \bar{d} = 1$.

8 Conclusions

In this article, we studied the weak imposition of boundary conditions for boundary element methods applied to 2D elastodynamics time-dependent problems. The proposed methods are particularly useful for mixed boundary value problems, where they allow the unified implementation of different conditions. The analysis carried out in this paper indicates that the considered approach is effective and reliable, giving results equivalent to those obtained by strong imposition of boundary data; as a drawback the number of degrees of freedom is doubled. As a second result, we observe that the EBEM in practice allows great flexibility for choosing the trial and test spaces of the discretization: in space variable, the displacement can be approximated by discontinuous elements in $L^2(\Gamma)$ and the same elements can be chosen for both displacement and traction.
The discussion in this article is restricted to the BIE (1) in terms of the single layer and double layer operators. The weak imposition of Neumann boundary conditions using (2) and mixed boundary conditions using (1)-(2), considering the full Calderón projector, is currently under investigation.

Acknowledgements. This work has been partially supported by the University of Parma with the project Fil2020 - Action A1 “Time-domain Energetic BEM for elastodynamic problems, with advanced applications”.

Appendix A Energy identity

The energy identity (19) comes from the integration, over the domain Ω and the time interval $[0,T]$, of the scalar product between Eq. (4) and $\dot{\mathbf{u}}$, i.e.

$$\begin{aligned} 0 &= \int_0^T \int_\Omega \sum_{h,k,l,i=1}^{2} \frac{\partial}{\partial x_h}\left(\mathcal{C}_{ih}^{kl}\frac{\partial u_k}{\partial x_l}(\mathbf{x},t)\right)\dot{u}_i(\mathbf{x},t) - \rho\sum_{i=1}^{2}\ddot{u}_i(\mathbf{x},t)\dot{u}_i(\mathbf{x},t)d\mathbf{x}dt = \\ &= \int_0^T \int_\Omega \sum_{h,k,l,i=1}^{2} \frac{\partial}{\partial x_h}\left(\mathcal{C}_{ih}^{kl}\frac{\partial u_k}{\partial x_l}(\mathbf{x},t)\right)\dot{u}_i(\mathbf{x},t) - \frac{\rho}{2}\frac{\partial}{\partial t}\sum_{i=1}^{2}\dot{u}_i^2(\mathbf{x},t)d\mathbf{x}dt\,. \end{aligned}$$

Integrating by parts and applying the null initial conditions, we obtain

$$0 = \int_0^T \left\{ \int_\Gamma \sum_{h,k,l,i=1}^{2}\left(\mathcal{C}_{ih}^{kl}\frac{\partial u_k}{\partial x_l}(\mathbf{x},t)n_h(\mathbf{x})\right)\dot{u}_i(\mathbf{x},t) - \int_\Omega \sum_{h,k,l,i=1}^{2}\left(\mathcal{C}_{ih}^{kl}\frac{\partial u_k}{\partial x_l}(\mathbf{x},t)\right)\frac{\partial \dot{u}_i}{\partial x_h}(\mathbf{x},t)\right\}d\mathbf{x}dt - \frac{\rho}{2}\int_\Omega\sum_{i=1}^{2}\dot{u}_i^2(\mathbf{x},T)d\mathbf{x},$$

Then, remembering the definition of traction (9) and applying the symmetry property of Hooke tensor, from the equality

$$0 = \int_0^T \left\{ \int_\Gamma \sum_{i=1}^{2} p_i(\mathbf{x},t)\dot{u}_i(\mathbf{x},t) - \int_\Omega \sum_{h,k,l,i=1}^{2}\frac{1}{2}\frac{\partial}{\partial t}\left(\mathcal{C}_{ih}^{kl}\frac{\partial u_k}{\partial x_l}(\mathbf{x},t)\frac{\partial u_i}{\partial x_h}(\mathbf{x},t)\right)\right\}d\mathbf{x}dt - \frac{\rho}{2}\int_\Omega\sum_{i=1}^{2}\dot{u}_i^2(\mathbf{x},T)d\mathbf{x}$$

we can conclude that

$$\frac{1}{2}\sum_{i=1}^{n}\left\{\int_\Omega \rho\dot{u}_i^2(\mathrm{x},T)dx + \int_\Omega \sum_{h,k,l=1}^{n}\mathcal{C}_{ih}^{kl}\frac{\partial u_k}{\partial y_l}(\mathbf{x},T)\frac{\partial u_i}{\partial y_h}(\mathbf{x},T)d\mathbf{x}\right\} = \sum_{i=1}^{n}\int_0^T\int_\Gamma p_i(\mathbf{x},t)\dot{u}_i(\mathbf{x},t)d\mathbf{x}dt.$$

Appendix B Element by element integration of double layer potential

In this appendix we briefly describe the numerical treatment of the integral element (31), furnishing the fundamentals for an efficient and precise computation of the discretized double layer potential $\mathbb{K}$. Due to the compact support of $w_m^{\mathbf{u}}(\boldsymbol{\xi})$ and $w_{\widetilde{m}}^{\mathbf{p}}(\mathbf{x})$, we follow an *element by element* approach, under which we need to focus on the approximation of the contribution given considering two generic mesh segments e_m and $e_{\widetilde{m}}$:

$$\int_{e_{\widetilde{m}}}\int_{e_m} w_m^{\mathbf{u}}(\boldsymbol{\xi})w_{\widetilde{m}}^{\mathbf{p}}(\mathbf{x})\widehat{\nu}_{ij}(r,\Delta)d\Gamma_{\boldsymbol{\xi}}d\Gamma_{\mathbf{x}}. \tag{60}$$

Thanks to the parametrization in arc length of e_m and $e_{\widetilde{m}}$ ($\mathbf{x}\in e_{\widetilde{m}} \rightleftharpoons s\in[0,\Delta x_{\widetilde{m}}]$, $\boldsymbol{\xi}\in e_m \rightleftharpoons z\in[0,\Delta x_m]$) we discover that (60) corresponds to the integral on the rectangular domain $[0,\Delta x_{\widetilde{m}}]\times[0,\Delta x_m]$:

$$\int_0^{\Delta x_{\widetilde{m}}}\fint_0^{\Delta x_m} w_m^{\mathbf{u}}(z)w_{\widetilde{m}}^{\mathbf{p}}(s)\widehat{\nu}_{ij}(r(s,z),\Delta)dzds, \tag{61}$$

where, with an abuse of notation, the shape functions $w_m^{\mathbf{u}}$ and $w_{\widetilde{m}}^{\mathbf{p}}$ are indicated with direct dependence on the local variables s and z and the inner integral is intended as a *Cauchy principal Value*.

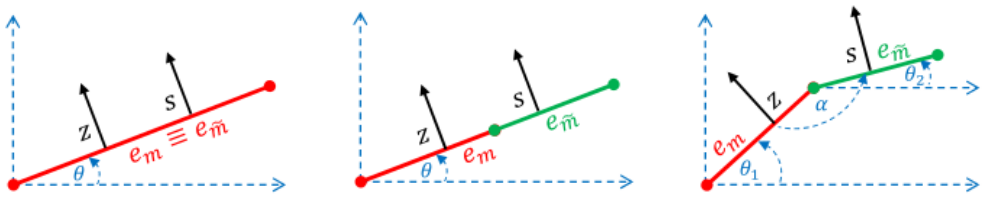

Figure 17: Configuration of the integration elements that allows the cancellation of the distance r: coincident elements (a), consecutive and aligned elements (b), consecutive and non-aligned elements (c).

In Figure 17 three possible configurations that can give a strongly singular integral are shown (for

simplicity, we just discuss the case "e_m on the left" for Figures 17(b) and 17(c)). The positions of the elements e_m and $e_{\widetilde{m}}$ determine the definition of the kernel $\widehat{\nu}_{ij}$, forcing us to differentiate the manipulation of (61) to get its numerical approximation, as indicated in Subsections B.1, B.2 and B.3.

Remark: the mutual position of e_m and $e_{\widetilde{m}}$ does not only determine the form of kernel $\widehat{\nu}_{ij}$ in local variables, but also affects the shape of the integration domain of (61), which, due the discontinuous Heaviside functions in definition (32), actually corresponds to the intersection $[0, \Delta x_{\widetilde{m}}] \times [0, \Delta x_m] \cap \{r(s,z) < c_P\Delta\}$. To improve the integral approximation despite the discontinuity of the kernel, this domain has to be divided in portions where the values of $H[c_S\Delta - r]$ and $H[c_P\Delta - r]$ are well determined. For further details about this splitting technique, which is outside the purpose of the paper but nevertheless remains crucial for the algorithmical implementation of the method, the interested reader is referred to [2].

In order to proceed with the manipulation of the local integral (61), we define the parameters

$$\sigma_1 = \cos(\theta) \quad \text{and} \quad \sigma_2 = \sin(\theta),$$

for coincident and consecutive aligned elements, while we set

$$\tau_{1i} = \cos(\theta_i) \quad \text{and} \quad \tau_{2i} = \sin(\theta_i), \quad i = 1, 2$$

for consecutive and non-aligned elements. This allows to differentiate the definition of the distance r w.r.t. the configurations identified in Figure 17:

- coincident elements: $r = |s - z|$ and $r_j = \sigma_j(s - z)$ for $j = 1, 2$;
- consecutive and aligned elements: $r = \Delta x_m - z + s$ and $r_j = \sigma_j r$ for $j = 1, 2$;
- consecutive and non-aligned elements: $r^2 = (\Delta x_m - z)^2 + s^2 - 2\cos(\alpha)(\Delta x_m - z)s$ and $r_j = \tau_{j1}(\Delta x_m - z) + \tau_{j2}s$ for $j = 1, 2$.

In the following, we only focus on the integration on the part of domain where $0 \le r \le c_S\Delta$, where in fact the strong singularity, for $r = 0$, of $\widehat{\nu}_{ij}$ is revealed, as indicated in (35). Outside $[0, \Delta x_{\widetilde{m}}] \times [0, \Delta x_m] \cap \{r(s,z) < c_S\Delta\}$ the integral is regular and does not require a particular treatment for its approximation. Therefore, it is useful to deduce the following inequalities for the inner variable $z \in [0, \Delta x_m]$:

- coincident elements: $r \le c_S\Delta \iff M(s) \le z \le m(s)$ with $M(s) = \max\{0, s - c_S\Delta\}$ and $m(s) = \min\{0, s + c_S\Delta\}$;
- consecutive and aligned elements: $r \le c_S\Delta \iff M(s) \le z \le \Delta x_m$ with $M(s) = \max\{0, s + \Delta x_m - c_S\Delta\}$;
- consecutive and non-aligned elements: $r \le c_S\Delta \iff M(s) \le z \le \Delta x_m$ with $M(s) = \max\left\{0, \Delta x_m - s\cos(\alpha) - \sqrt{c_S^2\Delta^2 - s^2\sin^2(\alpha)}\right\}$ (only for $\alpha \in [\pi/2, \pi]$).

In the considered portion of integration domain, it is moreover convenient to localize the points (s, z) for which $r(s, z) = 0$, corresponding, for the coincident elements case, to the axis $s = z$ and to the single point $(0, \Delta x_m)$ for all the other cases.

For the sake of simplicity, in the following subsections we identify with $f_{s,\Delta}(s, z)$ one of the functions

$$f(s,z) = \sqrt{c_S^2\Delta^2 - r(s,z)^2} \quad \text{or} \quad f(s,z) = \frac{1}{c_P\sqrt{c_S^2\Delta^2 - r(s,z)^2} + c_S\sqrt{c_P^2\Delta^2 - r(s,z)^2}},$$

which are continuous in $r(s, z) = c_S\Delta$ but not differentiable. The reduced double layer kernel (35) depends on both them. This could cause a reduction of precision in the approximation of (61), performed by quadrature formulas of Gaussian type, but a solution for this issue will be provided in the following.

B.1 Integration on coincident elements

To compute (61) for this configuration, due to the definition of r and of the generic component r_i in local variables it is worthwhile to consider the integral contribution

$$\mathcal{I} = \int_a^b \fint_{M(S)}^{m(s)} \frac{w_{\widetilde{m}}^{\mathbf{p}}(s) w_m^{\mathbf{u}}(z) f(s,z)}{s-z} dz ds \tag{62}$$

characterized by an integration domain $[a,b] \times [M(S), m(s)]$ having a not trivial intersection with the axis $s = z$. To compute (62), we perform a Taylor expansion of the numerator centred in $z = s$, allowing us to manipulate $\mathcal{I}$ as follows:

$$\begin{aligned}\mathcal{I} = &\int_a^b \int_{M(S)}^{m(s)} \frac{w_{\widetilde{m}}^{\mathbf{p}}(s)(w_m^{\mathbf{u}}(z) f(s,z) - w_m^{\mathbf{u}}(s) f(s,s))}{s-z} dz ds \\ &+ \int_a^b w_{\widetilde{m}}^{\mathbf{p}}(s) w_m^{\mathbf{u}}(s) f(s,s) \fint_{M(S)}^{m(s)} \frac{1}{s-z} dz ds = \mathcal{I}_1 + \mathcal{I}_2.\end{aligned}$$

Since the numerator of the integrand function is $\mathcal{O}(s-z)$, integral $\mathcal{I}_1$ is regular for $z = s$: this permits us to calculate it, both for the inner and the outer integration, using the Gauss-Legendre rule defined in (66). If $M(S) \neq 0$ or $m(s) \neq \Delta x_m$, integration on z can be improved combining rule (66) with the smoothing transformation (67), that, as stated in Appendix C, helps to regularize the integrand function at the extreme of the integration interval. Concerning $\mathcal{I}_2$, inner integration can be performed analytically as a Cauchy Principal Value:

$$\mathcal{I}_2 = \int_a^b w_{\widetilde{m}}^{\mathbf{p}}(s) w_m^{\mathbf{u}}(s) f(s,s) \left[\log\left(s - M(s)\right) - \log\left(m(s) - s\right)\right] ds.$$

It remains to approximate $\mathcal{I}_2$ as an integral in ds, which can be done using formula (66).

B.2 Integration on consecutive and aligned elements

The procedure is very similar to the one shown for coincident elements. The integral contribution

$$\mathcal{I} = \int_0^b \fint_{M(S)}^{\Delta x_m} \frac{w_{\widetilde{m}}^{\mathbf{p}}(s) w_m^{\mathbf{u}}(z) f(s,z)}{s + \Delta x_m - z} dz ds \tag{63}$$

is on a region of the integration domain containing the only singular point $(s,z) = (0, \Delta x_m)$. Again, we rewrite (63) by adding and subtracting terms that help with the regularization of the integrad function at the singular point, obtaining the equality

$$\begin{aligned}\mathcal{I} = &\int_0^b \int_{M(S)}^{\Delta x_m} \frac{w_{\widetilde{m}}^{\mathbf{p}}(s) w_m^{\mathbf{u}}(z) f(s,z) - w_m^{\mathbf{u}}(\Delta x_m) f(0, \Delta x_m))}{s + \Delta x_m - z} dz ds \\ &+ \int_0^b w_{\widetilde{m}}^{\mathbf{p}}(s) w_m^{\mathbf{u}}(\Delta x_m) f(0, \Delta x_m) \fint_{M(S)}^{\Delta x_m} \frac{1}{s + \Delta x_m - z} dz ds = \mathcal{I}_1 + \mathcal{I}_2.\end{aligned}$$

The regular integral $\mathcal{I}_1$ can be approximated by employing a standard Gauss-Legendre rule (combined with transformation (67) if $M(s) \neq 0$). The inner integral of $\mathcal{I}_2$ is computed analytically, giving

$$\mathcal{I}_2 = \int_0^b w_{\widetilde{m}}^{\mathbf{p}}(s) w_m^{\mathbf{u}}(s) f(s,s) \left[\log\left(\Delta x_m - M(s) + s\right) - \log\left(s\right)\right] ds.$$

Outer integration of $\mathcal{I}_2$ is performed by the Gaussian rule (66).

B.3 Integration on consecutive and non-aligned elements

In case of consecutive and non-aligned elements, due to the dependence of the integral kernels on the terms r_i/r or $r_i r_j r_k / r^3$ and their definition w.r.t the local variables s, z, we have to face two types of

integrals in order to compute (61):

$$\mathcal{I} = \int_0^b \fint_{M(S)}^{\Delta x_m} \frac{w^{\mathbf{p}}_{\widetilde{m}}(s) w^{\mathbf{u}}_m(z) f(s,z)(as + b(\Delta x_m - z))}{s^2 + (\Delta x_m - z)^2 - 2\cos(\alpha) s(\Delta x_m - z)} dz ds, \tag{64}$$

$$\widetilde{\mathcal{I}} = \int_0^b \fint_{M(S)}^{\Delta x_m} \frac{w^{\mathbf{p}}_{\widetilde{m}}(s) w^{\mathbf{u}}_m(z) f(s,z) p(s,z)}{\left(s^2 + (\Delta x_m - z)^2 - 2\cos(\alpha) s(\Delta x_m - z)\right)^2} dz ds, \tag{65}$$

where the function $p(s,z)$ in (65) is a polynomial of degree 3 in the variables s and z. We go on illustrating only the manipulation of integral (64), since the procedure for (65) is analogous:

$$\begin{aligned}
\mathcal{I} = &\int_0^b \int_{M(S)}^{\Delta x_m} \frac{w^{\mathbf{p}}_{\widetilde{m}}(s)(as + b(\Delta x_m - z)) \left[w^{\mathbf{u}}_m(z) f(s,z) - w^{\mathbf{u}}_m(\Delta x_m) f(0, \Delta x_m)\right]}{s^2 + (\Delta x_m - z)^2 - 2\cos(\alpha) s(\Delta x_m - z)} dz ds \\
&+ \int_0^b w^{\mathbf{p}}_{\widetilde{m}}(s) w^{\mathbf{u}}_m(\Delta x_m) f(0, \Delta x_m) as \fint_{M(S)}^{\Delta x_m} \frac{1}{s^2 + (\Delta x_m - z)^2 - 2\cos(\alpha) s(\Delta x_m - z)} dz ds \\
&+ \int_0^b w^{\mathbf{p}}_{\widetilde{m}}(s) w^{\mathbf{u}}_m(\Delta x_m) f(0, \Delta x_m) b \fint_{M(S)}^{\Delta x_m} \frac{\Delta x_m - z}{s^2 + (\Delta x_m - z)^2 - 2\cos(\alpha) s(\Delta x_m - z)} dz ds = \mathcal{I}_1 + \mathcal{I}_2 + \mathcal{I}_3.
\end{aligned}$$

Now the term $\mathcal{I}_1$ has a smooth integrand for $s = 0$ and $z = \Delta x_m$, therefore it can be approximated as done for the contributions of the same type in Subsections B.1-B.2. Contributions $\mathcal{I}_2$ and $\mathcal{I}_3$ can instead be calculated analytically in dz, giving rise to the following integrals in the outer variable s:

$$\mathcal{I}_2 = -\int_0^b w^{\mathbf{p}}_{\widetilde{m}}(s) w^{\mathbf{u}}_m(\Delta x_m) f(0, \Delta x_m) \frac{a}{\sin(\alpha)} \left[\arctan\left(-\frac{\cos(\alpha)}{\sin(\alpha)}\right) - \arctan\left(\frac{\Delta x_m - M(s) - s\cos(\alpha)}{s\sin(\alpha)}\right)\right] ds,$$

$$\begin{aligned}
\mathcal{I}_3 = -\int_0^b w^{\mathbf{p}}_{\widetilde{m}}(s) w^{\mathbf{u}}_m(\Delta x_m) f(0, \Delta x_m) b \Bigg[&\frac{1}{2}\log\left(\frac{s^2}{s^2 + (\Delta x_m - M(s))^2 - 2\cos(\alpha) s(\Delta x_m - M(s))}\right) \\
&+ \frac{\cos(\alpha)}{\sin(\alpha)}\left(\arctan\left(-\frac{\cos(\alpha)}{\sin(\alpha)}\right) - \arctan\left(\frac{\Delta x_m - M(s) - s\cos(\alpha)}{s\sin(\alpha)}\right)\right)\Bigg] ds.
\end{aligned}$$

The regularity of the integrand functions in $\mathcal{I}_2$ and $\mathcal{I}_3$ allows us to compute them employing formula (66).

Appendix C

The core of the algorithmic implementation of the EBEM is the computation of the integral elements (29) and (31), for which we extensively make use of the well known *Gauss-Legendre* quadrature formula, valid for any continuous function f in the interval $[-1, 1]$:

$$\int_{-1}^{1} f(z) dz = \sum_{k=0}^{n} \omega_{G,k} f(z_k) + R_{G,n}(f), \tag{66}$$

where $R_{G,n}(f)$ is the reminder of the formula. This quadrature rule, of interpolatory type and with degree of accuracy $2n+1$, fits well the purpose of an accurate approximation of the integrals reported in Appendix B. A definitions of the nodes z_k and the weights $\omega_{G,k}$, depending on the properties of the Legendre polynomials, can be found in [19].
In the Appendix B we have also to deal with functions characterized by an infinite gradient at the endpoints of integration intervals. The approximation of such kind of integrals using (66) is possible, however a good precision can be reached as long as a great amount of quadrature nodes is set. To overcome this issue, we combine formula (66) with the smoothing transformation $\Theta_{p,q} : [0,1] \to [0,1]$:

$$\Theta_{p,q}(t) = \frac{(p+q-1)!}{(p-1)!(q-1)!} \int_0^t u^{p-1}(1-u)^{q-1} du, \quad t \in [0,1],\ p, q \geq 1. \tag{67}$$

To explain the use of this regularization, we consider the integral of a generic function f in the interval $[0,1]$ and we dispose the change of variable $z = \Theta_{p,q}(t)$, as follows:

$$\int_0^1 f(z) dz = \int_0^1 f\left(\Theta_{p,q}(t)\right) \Theta'_{p,q}(t) dt, \tag{68}$$

then we approximate by Gaussian rule (66), after a suitable transformation of the integration interval, the left hand side of (68). As discussed in [18], the purpose of this strategy is to accumulate the quadrature nodes near the integration endpoints, according to the values of the positive parameters p and q as shown in Figure 18. This helps to improve the approximation of the integral, while avoiding a potential increase of the computational costs in the quadrature procedure.

Remark: the integrals listed in Appendix B.1,B.2 and B.3 are always approximated setting in formula (66) 64 nodes, in order to globally compute with single precision accuracy the entries of the Toeplitz matrix (28).

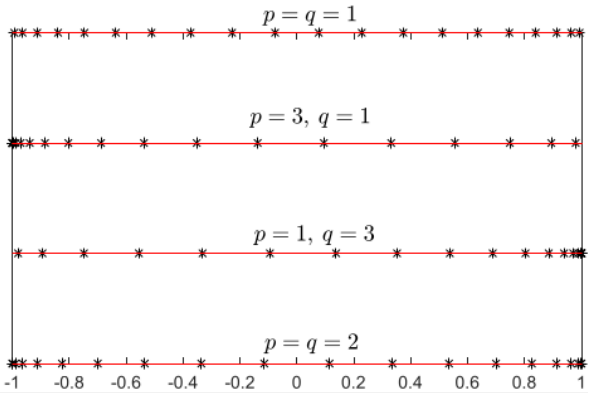

Figure 18: Position of the 20 nodes of the Gauss-Legendre formula according to the application of the smoothing transformation $\Theta_{p,q}$ for different values of p and q.

References

[1] A. Aimi, L. Desiderio, M. Diligenti, and C. Guardasoni. Application of energetic BEM to 2D elastodynamic soft scattering problems. *Communications in Applied and Industrial Mathematics*, 10(1):182–198, 2019.

[2] A. Aimi, G. Di Credico, M. Diligenti, and C. Guardasoni. Highly accurate quadrature schemes for singular integrals in energetic BEM applied to elastodynamics. *J. Comput. Appl. Math.*, 410:Paper No. 114186, 27, 2022.

[3] A. Aimi, G. Di Credico, H. Gimperlein, and E. P. Stephan. Higher-order time domain boundary elements for elastodynamics - graded meshes and hp-versions. *Numerische Mathematik*, doi:10.1007/s00211-023-01355-x.

[4] A. Aimi, G. Di Credico, and C. Guardasoni. Energetic Galerkin Boundary Element Method for 2D elastodynamics: Integral operators with weak and strong singularities. *WIT Transactions on Engineering Sciences*, 131:17–29, 2021.

[5] A. Aimi, M. Diligenti, and C. Guardasoni. Numerical integration schemes for applications of energetic Galerkin BEM to wave propagation problems. *Riv. Math. Univ. Parma (N.S.)*, 2(1):147–187, 2011.

[6] A. Aimi, M. Diligenti, C. Guardasoni, and I. Mazzieri. An energy approach to space-time Galerkin BEM for wave propagation problems. *Internat. J. Numer. Methods Engrg.*, 80:1196–1240, 2009.

[7] L. Banz, H. Gimperlein, Z. Nezhi, and E. P. Stephan. Time domain BEM for sound radiation of tires. *Computational Mechanics*, 58:45–57, 2016.

[8] T. Betcke, E. Burman, and M. W. Scroggs. Boundary Element Methods with weakly imposed boundary conditions. *SIAM J. Sci. Comput.*, 41:A1357–A1384, 2019.

[9] T. Betcke, E. Burman, and M. W. Scroggs. Boundary element methods for helmholtz problems with weakly imposed boundary conditions. *SIAM Journal on Scientific Computing*, 44(5):A2895–A2917, 2022.

[10] E. Burman, S. Frei, and M. W. Scroggs. Weak imposition of Signorini boundary conditions on the Boundary Element Method. *SIAM J. Numer. Anal.*, 58:2334–2350, 2020.

[11] Z. Chen and Y. Xu. The Petrov–Galerkin and iterated Petrov–Galerkin methods for second-kind integral equations. *SIAM Journal on Numerical Analysis*, 35(1):406–434, 1998.

[12] M. Costabel and F. J. Sayas. Time-dependent problems with the boundary integral equation method. *Encyclopedia of Computational Mechanics*, 1:703–721, 2004.

[13] S. Falletta, G. Monegato, and L. Scuderi. Two boundary integral equation methods for linear elastodynamics problems on unbounded domains. *Computers & Mathematics with Applications*, 78(12):3841–3861, 2019.

[14] A. Frangi. Elastodynamic by BEM: a new direct formulation. *Int. J. Numer. Meth. Engng.*, 45:721–740, 1999.

[15] H. Gimperlein, M. Maischak, and E. P. Stephan. Adaptive time domain boundary element methods with engineering applications. *Journal of Integral Equations and Applications*, 29(1):75–105, 2017.

[16] H. Gimperlein, F. Meyer, C. Özdemir, D. Stark, and E. P. Stephan. Boundary elements with mesh refinements for the wave equation. *Numerische Mathematik*, 139:867–912, 2018.

[17] T. Ha-Duong. On retarded potential boundary integral equations and their discretisation. In *Topics in computational wave propagation*, pages 301–336. Springer, 2003.

[18] G. Monegato and L. Scuderi. Numerical integration of functions with boundary singularities. *Journal of Computational and Applied Mathematics*, 112:201–214, 1999.

[19] A. Quarteroni. Modellistica numerica per problemi differenziali, 4th edition. *Springer Science & Business Media*, 2009.

[20] F. J. Sayas. *Retarded potentials and time domain boundary integral equations: A road map*, volume 50. Springer, 2016.

[21] R. Stenberg. On some techniques for approximating boundary conditions in the finite element method. *Journal of Computational and applied Mathematics*, 63(1-3):139–148, 1995.